



CAN UNCLASSIFIED



DRDC | RDDC
technologysciencetechnologie

Constitutive models investigation to simulate damage/failure of Aluminium (Al) 6061-T6

Patrick Leclerc
Genevière Toussaint
DRDC – Valcartier Research Centre

Defence Research and Development Canada

Scientific Report

DRDC-RDDC-2018-R198

November 2018

CAN UNCLASSIFIED

CAN UNCLASSIFIED

IMPORTANT INFORMATIVE STATEMENTS

This document was reviewed for Controlled Goods by Defence Research and Development Canada (DRDC) using the Schedule to the *Defence Production Act*.

Disclaimer: Her Majesty the Queen in right of Canada, as represented by the Minister of National Defence ("Canada"), makes no representations or warranties, express or implied, of any kind whatsoever, and assumes no liability for the accuracy, reliability, completeness, currency or usefulness of any information, product, process or material included in this document. Nothing in this document should be interpreted as an endorsement for the specific use of any tool, technique or process examined in it. Any reliance on, or use of, any information, product, process or material included in this document is at the sole risk of the person so using it or relying on it. Canada does not assume any liability in respect of any damages or losses arising out of or in connection with the use of, or reliance on, any information, product, process or material included in this document.

Endorsement statement: This publication has been peer-reviewed and published by the Editorial Office of Defence Research and Development Canada, an agency of the Department of National Defence of Canada. Inquiries can be sent to: Publications.DRDC-RDDC@drdc-rddc.gc.ca.

Abstract

The design of a military vehicle is a complex science that requires the careful consideration of factors, such as armour protection that is essential for survivability, while considering the need to conceive a lightweight and economical vehicle. Therefore, predicting the material behavior and damage until failure is of primary importance when evaluating the vulnerability of military platforms and could influence the optimization of protection systems. In this report, the aim is to investigate the effect of modifying several constitutive and damage models that could be used to simulate the damage behavior of Aluminium (Al) 6061-T6 using the LS-DYNA hydrocode. Several models are compared numerically and their strengths/weaknesses are presented. The Johnson-Cook constitutive model and GISSMO damage models were combined and the effects of varying several parameters are presented. Since defence applications involve several failure modes, further studies should be performed to investigate the material response under various triaxialities and the mesh dependency in order to simulate accurately the damage/failure of Aluminium 6061-T6.

Significance to defence and security

The development of novel concepts and designs of military platforms is increasingly becoming dependant on modeling and simulations that are performed to support their development. Therefore, it becomes essential to predict adequately the damage and failure that occur in the materials. The modeling of the evolution of damage and failure is a challenge itself as it depends, for example, on the mechanical and thermal properties of each material, their sensitivity to the strain rates and temperatures, and how they are dynamically solicited. The development of an accurate damage and failure model is thus very important when evaluating the dynamic behavior of military protection systems under extreme loads such as against threats effects.

Résumé

La conception d'un véhicule militaire est une science complexe qui requiert un examen approfondi de facteurs, tels que l'armure de protection qui est essentiel à la surviabilité, tout en considérant le besoin de concevoir un véhicule léger et économique. C'est pourquoi, prédire le comportement et le dommage jusqu'à la rupture des matériaux est de première importance lorsqu'on évalue la vulnérabilité de plateformes militaires et peut ainsi influencer l'optimisation des systèmes de protection. Dans ce rapport, l'objectif est d'investiguer plusieurs modèles constitutifs et d'endommagement qui pourraient être utilisés pour simuler l'endommagement de l'Aluminium 6061-T6 avec l'hydrocode LS-DYNA. Plusieurs modèles sont comparés numériquement et leurs forces/faiblesses sont présentées. Le modèle constitutif de Johnson-Cook a été combiné au modèle d'endommagement de GISSMO et l'effet de varier la valeur de plusieurs paramètres est présenté. Étant donné que les applications militaires impliquent plusieurs modes de rupture, des études complémentaires devraient être réalisées pour investiguer la réponse du matériau soumis à des triaxialités différentes et la dépendance au maillage dans le but de simuler adéquatement l'endommagement/rupture de l'Aluminium 6061-T6.

Importance pour la défense et la sécurité

Le développement de nouveaux concepts et la conception de plateformes militaires sont de plus en plus dépendants de la modélisation et simulations qui sont effectuées pour appuyer leur développement. C'est pourquoi, il devient essentiel de prédire adéquatement le dommage et la rupture qui se produit dans les matériaux. La modélisation de l'évolution du dommage et la rupture est un défi en soi parce qu'elle dépend, par exemple, des propriétés mécaniques et thermiques de chaque matériau, de leur sensibilité au taux de déformation, à la température, et comment ils sont sollicités dynamiquement. Le développement d'un modèle d'endommagement et de rupture fidèle est donc très important lorsqu'on évalue le comportement en dynamique de systèmes de protection contre les effets des menaces.

Table of contents

Abstract	i
Significance to defence and security	i
Résumé	ii
Importance pour la défense et la sécurité	ii
Table of contents	iii
List of figures	v
List of tables	vi
Acknowledgements	vii
1 Introduction	1
2 Literature review.	2
2.1 Equations of conservation	2
2.1.1 Mass equation.	3
2.1.2 Momentum equation	3
2.1.3 Energy equation	3
2.2 Stress and strain calculations	4
2.3 Equations of state	6
2.4 Constitutive, damage and failure models.	6
2.4.1 Elastic plastic model	6
2.4.2 Johnson-Cook model	7
2.4.2.1 Step 1: Quasi-static tensile test	8
2.4.2.2 Step 2: Variable triaxiality tests.	9
2.4.2.3 Step 3: Effect of strain rate	9
2.4.2.4 Step 4: Effect of temperature.	11
2.4.3 Zerilli-Armstrong model	13
2.4.4 Cockcroft-Latham Ductile failure criterion	15
2.4.5 GISSMO—Generalized Incremental Stress State dependent damage MOdel.	16
2.4.6 DIEM—Damage Initiation and Evolution Model.	17
3 Summary of Giglio et al. experimentation [2]	20
4 Numerical simulations	22
4.1 Simulations using the mat_plastic_kinematic constitutive model	22
4.1.1 First trials: Varying the hardening parameter	23
4.1.2 Second trials: Varying the tangent modulus	24
4.2 Simulations with mat_johnson_cook constitutive model	26
4.2.1 First Trials: Evaluating effect of damage and erosion activation and desactivation.	27
4.2.2 Second trials: Influence of alternative D_4 parameter	29
4.2.3 Third trials: Adding a pressure cut-off value	29
4.2.4 Fourth Trials: Effects of EFMIN variation	30

4.3	Simulations with <i>mat_johnson_cook</i> and GISSMO (<i>mat_add_erosion</i>)	31
4.3.1	First trials: <i>mat_simplified_johnson_cook</i> true-stress/strain curves evaluated at different places along critical cross section	31
4.3.2	Second trials: Comparison of damage and Johnson-Cook type settings	32
4.3.3	Third trials: Adjusting the triaxiality failure curve to obtain the correct failure stress in tension	33
4.3.4	Fourth trials: Verifying virtual extensometer assumptions	33
4.3.5	Fifth trials: Verifying virtual extensometer assumptions	34
4.3.6	Sixth trials: Adjusting the size regulation factor	35
4.3.7	Seventh trials: Adjusting the fading exponent curve FADEXP	38
4.3.8	Eighth trials: Damage exponent variation	39
4.4	Summary of numerical simulations.	40
5	Conclusion	42
	References	43
	List of symbols/abbreviations/acronyms/initialisms	46

List of figures

Figure 1:	Comparison between a) Lagrangian and b) Eulerian methods [3].	2
Figure 2:	Comparison of engineering and true stress-strain curves and their converted curves.. . . .	5
Figure 3:	Variation of Failure Strain with triaxiality extracted from [12].	9
Figure 4:	Stress-strain curves as a function of strain rate extracted from [12].	10
Figure 5:	Variation of stress with log of strain rate extracted from [12].	10
Figure 6:	Variation of failure strain with ln of strain rate extracted from [12].	10
Figure 7:	Stress-strain curves as a function of temperature extracted from [12].. . . .	12
Figure 8:	Graph plotted to find temperature constant m extracted from [12].	12
Figure 9:	Failure strain vs. dimensionless temperature to find D_5 parameter extracted from [12]..	13
Figure 10:	Experimental data and simulation results of samples failing at various strain rates ([17] extracted [20]).. . . .	14
Figure 11:	Schematic representation of the damage material area (S_D) and the intact material area (S)	17
Figure 12:	Andrade et al.'s findings showing that a well-calibrated GISSMO model is as effective as DIEM, extracted from [25].	19
Figure 13:	a) Round smooth specimen b) Round notched specimen (notch radius 12 mm) c) Round notched specimen (notch radius 5 mm) d) Pure tension and multiaxial specimen e) Upsetting specimen, extracted from [2].	21
Figure 14:	2D axisymmetric model of a tensile sample.	22
Figure 15:	Effect of the Beta Parameter (0, 0.13 and 1) using Giglio et al. experiments [2]. . . .	24
Figure 16:	Calibration of tangent modulus to Giglio experimental results.	25

List of tables

Table 1:	Linear polynomial equation of state parameters for Al 6061-T6 [8].	6
Table 2:	Johnson-Cook parameters for various materials ($\dot{\epsilon}_0=1s^{-1}$) extracted from Meyer [5]. . .	8
Table 3:	Evolution of instability (F) and damage (D) values during a tensile test.	17
Table 4:	Summary Giglio et al. experiments results [2].	20
Table 5:	Al 6061-T6 constitutive model constants.	23
Table 6:	Johnson-Cook constitutive model parameters.	27
Table 7:	Johnson-Cook damage model parameters.	27

Acknowledgements

Le travail a été effectué dans le cadre du projet Land Operational Vehicles (unité de travail 02ba.09) permettant ainsi à un étudiant sous-gradué d'obtenir de l'expérience pratique dans ce domaine.

This page intentionally left blank.

1 Introduction

The objective of this report is mainly to investigate the effect of modifying several constitutive and damage parameters on the numerical behavior of Aluminium (Al) 6061-T6 while using the LS-DYNA hydrocode [1] to perform the finite element simulations. Several parameters of the *mat_plastic_kinematic* and *mat_johnson_cook* constitutive models are evaluated as well as the effect of modifying several of these parameters when combining to a damage model. In the first section, a short description on hydrocodes is provided and the governing equations that are resolved during a simulation are provided. Then a literature review of various constitutive and damage models are presented. In the following section, a summary of experimental work extracted from [2] is presented. This work is used as a reference to compare with the simulations results obtained in the present study. The effects of many parameters are presented. The Johnson-Cook (JC) constitutive model and Generalized Incremental Stress State dependant damage MOdel (GISSMO) were combined and are proposed as a method to simulate the damage and failure of Al 6061-T6 when doing simulations with the LS-DYNA hydrocode. Finally, a conclusion and some recommendations are presented.

The following work was performed under the Land Operational Vehicles (LOV) project with the aim to provide traineeship and work experience to an undergraduate student.

2 Literature review

An hydrocode is a computational tool that allows modeling the behavior of a fluid at different velocities [3]. Therefore, hydrocodes are often used to study particular non-linear problems that are time-dependant. The material under study can be discretized (meshed) to approximate the geometry. In order to calculate the effect of internal and external forces applied to the geometry, it assumes the forces are constant over a short period of time, called time step, and the differential equations are resolved from the principles of conservation of momentum, mass and energy. An equation of state is also needed when the volumetric deformation is not negligible [4]. The equation of state defines the thermodynamic state relating pressure to other state variables such as density and internal energy (dependant on temperature for example).

In this literature review, Section 2.1 presents the equations of conservation, Section 2.2 explains stress and strain calculations, then Section 2.3 provides several equations of state, and finally Section 2.4 presents various constitutive, damage and failure models.

2.1 Equations of conservation

Conservation equations are traditionally represented in Eulerian or Lagrangian formulations. In the Lagrangian approach, the mesh follows the geometry in space, while in Eulerian approach, the frame of reference (mesh) is fixed in space and the material flows through the mesh. Lagrangian formulations are simple to resolve but are not well suited for high deformation problems, in that case, Eulerian formulations are prioritized. However, Eulerian formulations have other limitations. For instance, if there are two materials with two different constitutive equations, the same element will have different materials at different times, and it is thereof difficult to track the materials interface [4]. The Eulerian formulations have also a more limited spatial resolution. An example of Lagrangian and Eulerian materials was represented by Collins [1] and is shown in Figure 1. In Figure 1a, the dinosaur shape undergoes extreme deformation and the mesh become extremely distorted, while using an Eulerian approach, as shown in Figure 1b, the mesh remains fixed in space and the elements are not distorted.

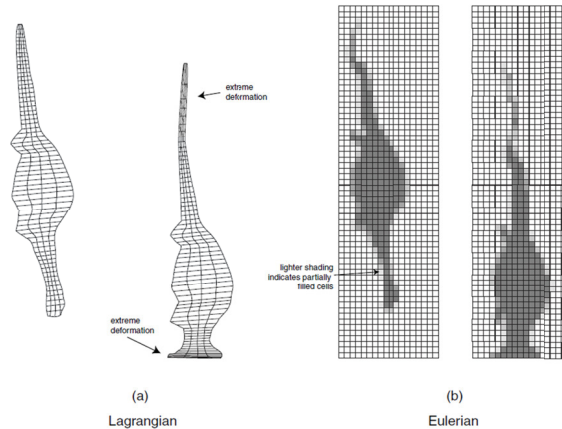


Figure 1: Comparison between a) Lagrangian and b) Eulerian methods [3].

New approaches combining both Lagrange and Eulerian methods have been developed and are called “Arbitrary Lagrangian-Eulerian” (ALE) and Simplified ALE (SALE). Combined models make it possible to solve problems involving both Lagrangian and Eulerian approaches in the same simulation. The conservation equations for both Lagrangian and Eulerian formulations are presented in the following sub-sections and were extracted from [5].

2.1.1 Mass equation

Eulerian:

$$\frac{\delta \rho}{\delta t} + \nabla \cdot (\rho \mathbf{u}) = 0 \quad (1)$$

Lagrangian:

$$\frac{D\rho}{Dt} + \rho \nabla \cdot \mathbf{u} = 0 \quad (2)$$

Where ρ is the density, \mathbf{u} is the volume of material flowing through a defined unit area and t is the time.

2.1.2 Momentum equation

Eulerian:

$$\rho \left(\frac{\delta \mathbf{u}}{\delta t} + \mathbf{u} \cdot \nabla \mathbf{u} \right) = -\nabla \mathbf{P} \quad (3)$$

Where ∇ corresponds to the gradient and \mathbf{P} the stresses.

Lagrangian:

$$\rho \frac{D\mathbf{u}}{Dt} = -\nabla \mathbf{P} \quad (4)$$

2.1.3 Energy equation

Eulerian:

$$\frac{\delta}{\delta t} \left(E + \frac{1}{2} u^2 \right) \rho + \nabla \cdot \left[\rho \left(E + \frac{1}{2} u^2 \right) \mathbf{u} + P \mathbf{u} \right] = 0 \quad (5)$$

Where u defines the velocity, P the pressure and E is the internal energy per unit mass.

Lagrangian:

$$\frac{dE}{dt} + P \frac{dV}{dt} = 0 \quad (6)$$

Where V corresponds to the volume.

2.2 Stress and strain calculations

The principal stresses in both 2D and 3D may be obtained by solving the roots of the following cubic equation [6]:

$$\sigma_p^3 - I_1 \sigma_p^2 + I_2 \sigma_p - I_3 = 0 \quad (7)$$

Where I are the stress invariants and where the three σ_p solutions are the three principal stresses $\sigma_1 \geq \sigma_2 \geq \sigma_3$, and:

$$I_1 = \sigma_x + \sigma_y + \sigma_z \quad (8)$$

$$I_2 = \sigma_x \sigma_y + \sigma_x \sigma_z + \sigma_y \sigma_z - \tau_{xy}^2 - \tau_{yz}^2 - \tau_{xz}^2 \quad (9)$$

$$I_3 = \sigma_x \sigma_y \sigma_z + \tau_{xy} \tau_{yz} \tau_{xz} - \sigma_x \tau_{yz}^2 - \sigma_y \tau_{xz}^2 - \sigma_z \tau_{xy}^2 \quad (10)$$

The ASM Handbook [7] defines the engineering stress σ_{eng} as the average longitudinal stress in the tensile specimen and is obtained by dividing the load applied F divided by the initial area A_0 as provided by Equation (11). The engineering strain ϵ_{eng} is obtained by dividing the variation of the gage length of the specimen δ by its original length L_0 .

$$\sigma_{eng} = \frac{F}{A_0} \quad (11)$$

$$\epsilon_{eng} = \frac{\delta}{L_0} = \frac{L - L_0}{L_0} \quad (12)$$

Where L is the current length.

True stress σ_{true} is given by:

$$\sigma_{true} = \sigma_{eng}(1 + \epsilon_{eng}) \quad (13)$$

Beyond the maximum load, the true stress corresponds to the load applied divided by the instantaneous area (A):

$$\sigma_{true} = \frac{F}{A} \quad (14)$$

The true strain ϵ_{true} is given by the log of current length L over the original length:

$$\epsilon_{true} = \ln\left(\frac{L}{L_0}\right) \quad (15)$$

This gives a better representation of the true stress condition given that necking occurs and the cross section varies significantly over the course of the application of a heavy load on a ductile material. Experimental data are often provided in the form of engineering stress and strain, and will need to be converted to true stress and strain to compare with simulation results. An example of comparison between the engineering and true stress-strain curves extracted from [7] for a tensile rod sample of Aluminium 6061-T6 is shown in Figure 2.

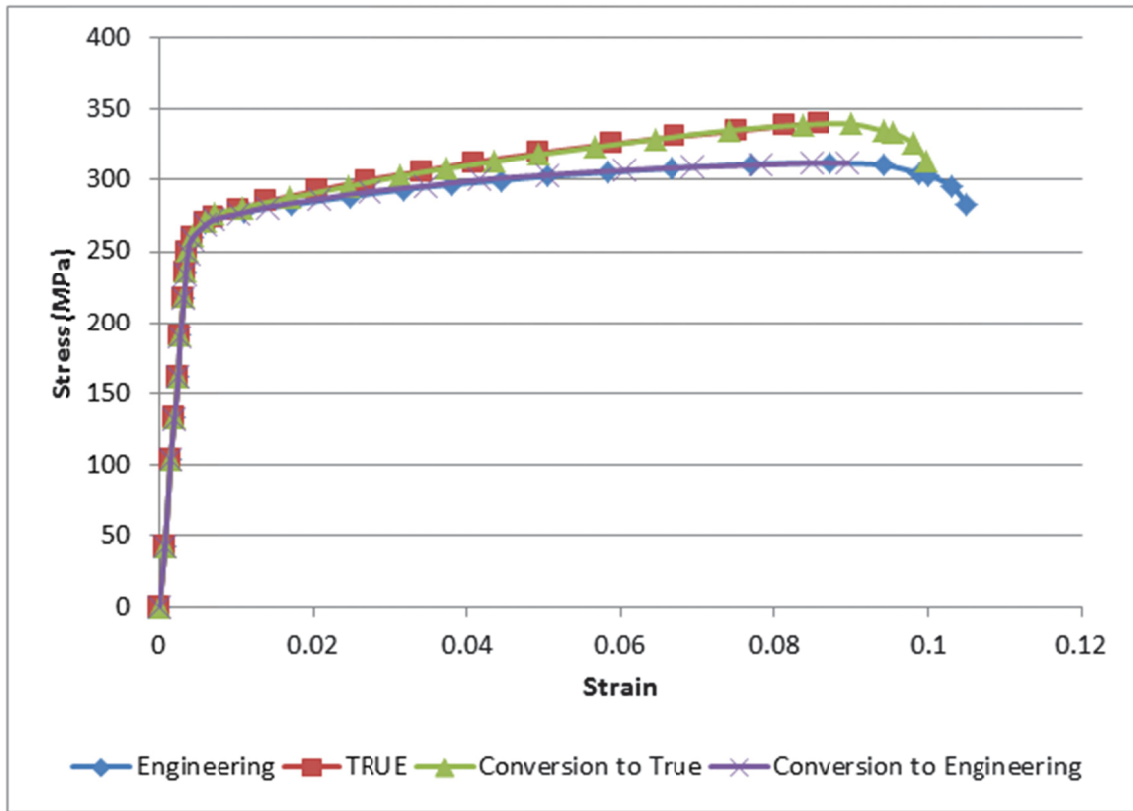


Figure 2: Comparison of engineering and true stress-strain curves and their converted curves.

2.3 Equations of state

As discussed previously, an Equation Of State (EOS) is required when the deformation of the material is non negligible compared to the pressure that is applied. It relates pressure to density and internal energy. It also accounts for changes in irreversible thermodynamic processes such as shock heating [1]. Examples of equations of states are provided in LS-DYNA [4] such as a *Linear polynomial* EOS, also when considering the shock velocity a *Mie-Grüneisen* or *Grüneisen* EOS can be defined, or when high explosives pressure of the detonation products need to be determined a *Jones-Wilkins-Lee* EOS can be used, an *Ideal gas* EOS when the pressure is determine in low density gas, etc.

The *linear polynomial* EOS was used in the simulations of this report. In the linear polynomial EOS, the Pressure (P) is given by:

$$P = C_0 + C_1\mu + C_2\mu^2 + C_3\mu^3 + (C_4 + C_5\mu + C_6\mu^2)E \quad (16)$$

Where:

$$\mu = \frac{\rho}{\rho_0} - 1 \quad (17)$$

And $\frac{\rho}{\rho_0}$ is the ratio of current density and reference density [4]. The C values are called the polynomial equation coefficients, and E corresponds to the internal energy per unit reference volume. The coefficients for the *linear polynomial* EOS used for Al 6061-T6 are given in Table 1 [6]:

Table 1: Linear polynomial equation of state parameters for Al 6061-T6 [8].

Parameter	C ₀	C ₁	C ₂	C ₃	C ₄	C ₅ , C ₆
Units	GPa	GPa	GPa	GPa		
Values	0	74.2	60.5	36.5	1.96	

2.4 Constitutive, damage and failure models

In order to model plastic deformation and ductile failure, constitutive models can be coupled or uncoupled. When plastic deformations and material damage calculations are coupled, failure occurs when a certain damage critical value is reached [9]. For uncoupled models, such as the Johnson-Cook material model [10], plastic deformation is calculated assuming no damage in the material. The failure criterion is based on the stress and strain histories and failure occurs when the critical value is reached [9].

2.4.1 Elastic plastic model

The *mat_plastic_kinematic* material model in the LS-DYNA hydrocode is a basic model which defines the behavior of the material model using two curves, one defining the elastic region of a material (also defined by the Young's modulus), and the other one defines the linear plastic behavior of the material from the yield stress to the ultimate tensile strength using a simplified representation of the plastic region, called ETAN. Element are deleted using a failure criteria once they exceed a given strain [4]. This failure strain does not necessarily directly correspond to the deformation at failure, because it is mesh dependant.

The plastic hardening modulus (E_h) is obtained using the Young's Modulus (E) and the tangent modulus (called ETAN or E_T) is calculated as follows [4, 11]:

$$E_T = \frac{E_h \cdot E}{E_h + E} \quad (18)$$

$$E_h = \frac{E_T \cdot E}{E - E_T} \quad (19)$$

$$E_h = \frac{\sigma_{true} - \sigma_y}{\epsilon_{true} - \frac{\sigma_{true}}{E}} \quad (20)$$

Where σ_y is defined by the stress at the yield point.

In addition, this model is capable of considering strain rate effects using the Cowper-Symonds model.

$$\frac{\sigma_{eff}}{\sigma_{static}} = 1 + \left(\frac{\dot{\epsilon}}{C} \right)^{\frac{1}{p}} \quad (21)$$

It is important to use the true stress and true strain curves and not the engineering stress and engineering strain curves when calibrating the parameters.

2.4.2 Johnson-Cook model

Johnson and Cook [10] proposed the following model consisting of experimentally determined constants σ_0 , B , C , n and m , which yields a Von Mises equivalent flow stress:

$$\sigma = (\sigma_0 + B\epsilon^n) \left(1 + C \ln \frac{\dot{\epsilon}}{\dot{\epsilon}_0} \right) [1 - (T^*)^m] \quad (22)$$

Where $\dot{\epsilon}_0$ is a reference strain rate which may be assumed equal to 1 for simplicity, ϵ is the effective plastic strain, and T^* is the unit-less temperature:

$$T^* = \frac{T - T_r}{T_m - T_r} \quad (23)$$

Where T_r is the reference temperature of the material (ambient temperature), and T_m is the melting temperature of the material.

The first set of brackets represents the strain sensitivity, the second represents strain rate sensitivity, and the final bracket group is temperature sensitivity.

Parameters for various materials are listed in Table 2.

Table 2: Johnson-Cook parameters for various materials ($\dot{\epsilon}_0 = 1s^{-1}$) extracted from Meyer [5].

Material	Values								
	Hardness	Density	Specific heat	Melting temperature	σ_0	B	n	C	m
	Rockwell	kg/m ³	J/kg·K	K	MPa	MPa			
OFHC Copper	F-30	8960	383	1356	90	292	0.31	0.025	1.09
Cartridge brass	F-67	8520	385	1189	112	505	0.42	0.009	1.68
Nickel 200	F-79	8900	446	1726	163	648	0.33	0.006	1.44
Armco iron	F-72	7890	452	1811	175	380	0.32	0.060	0.55
1006 steel	F-94	7890	452	1811	350	275	0.36	0.022	1.00
2024-T351 Aluminium	B-75	2770	875	775	265	426	0.34	0.015	1.00
7039 Aluminium	B-76	2770	875	877	337	343	0.41	0.010	1.00
4340 steel	C-30	7830	477	1793	792	510	0.26	0.014	1.03
S-7 tool steel	C-50	7750	477	1763	1539	477	0.18	0.012	1.00
Tungsten alloy (0,07Ni, 0,03Fe)	C-47	17000	134	1723	1506	177	0.12	0.016	1.00

The stress equation above will help produce a simulation that represents the elastic and plastic deformation of a material, but, it takes a failure equation to determine at what strain an element will fail in order for it to be deleted.

$$\epsilon_f = [D_1 + D_2 \exp(D_3 \sigma^*)][1 + D_4 \ln(\dot{\epsilon}_p^*)][1 + D_5 T^*] \quad (24)$$

In the first bracket, σ^* is the ratio of pressure over effective stress (triaxiality). In the second bracket, $\dot{\epsilon}_p^*$ is the effective plastic strain rate and T^* is the dimensionless temperature, as defined previously [4].

The following sub-section was extracted from [12] and presents an example of the steps to follow to determine the parameters from experimental data for an armour steel.

2.4.2.1 Step 1: Quasi-static tensile test

$$\sigma = (\sigma_0 + B\epsilon^n) \left(1 + C \ln \frac{\dot{\epsilon}}{\dot{\epsilon}_0}\right) [1 - (T^*)^m] \quad (25)$$

Room temperature
Low constant strain rate

A quasi-static tensile test must be conducted to determine the yield stress σ_0 , and the hardening parameters B and n which fulfill the requirements of the first bracket (strain sensitivity). B and n are obtained by doing a curve of best fit.

2.4.2.2 Step 2: Variable triaxiality tests

Conducting tensile and combined-loading tests on specimens to induce varying triaxialities shall make it possible to obtain parameters D_1 , D_2 , and D_3 for the first bracket group of the failure strain equation.

$$\epsilon_f = [D_1 + D_2 \exp(D_3 \sigma^*)][1 + D_4 \ln(\dot{\epsilon}_p^*)][1 + D_5 T^*] \quad (26)$$

$$\epsilon_f = \boxed{[D_1 + D_2 \exp(D_3 \sigma^*)]} \cancel{[1 + D_4 \ln(\dot{\epsilon}_p^*)]} \cancel{[1 + D_5 T^*]} \quad (27)$$

Low constant strain rate Room temperature

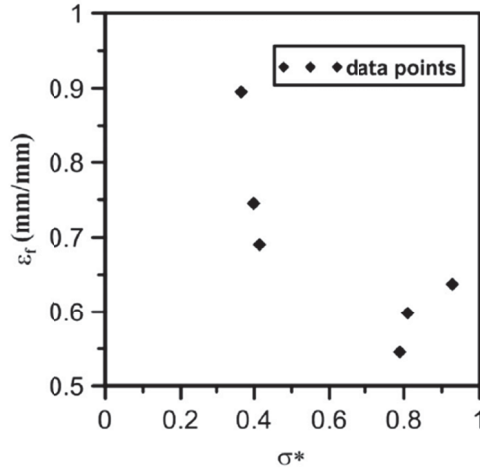


Figure 3: Variation of Failure Strain with triaxiality extracted from [12].

2.4.2.3 Step 3: Effect of strain rate

Variable strain rate tests are conducted to find C (second bracket of Equation (28)) and D_4 (second bracket of Equation (29)).

$$\sigma = \boxed{(\sigma_0 + B \epsilon^n)} \boxed{\left(1 + C \ln \frac{\dot{\epsilon}}{\dot{\epsilon}_0}\right)} \cancel{[1 - (T^*)^m]} \quad (28)$$

Known Negligible

$$\epsilon_f = \boxed{[D_1 + D_2 \exp(D_3 \sigma^*)]} \boxed{[1 + D_4 \ln(\dot{\epsilon}_p^*)]} \cancel{[1 + D_5 T^*]} \quad (29)$$

Known Negligible

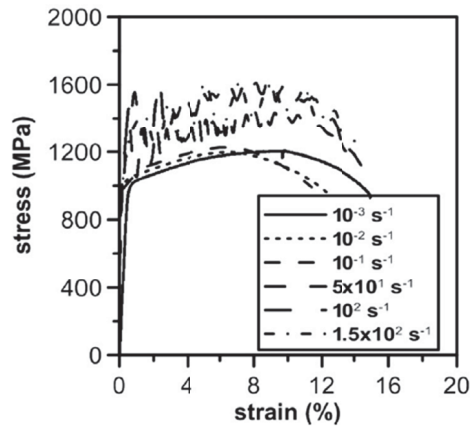


Figure 4: Stress-strain curves as a function of strain rate extracted from [12].

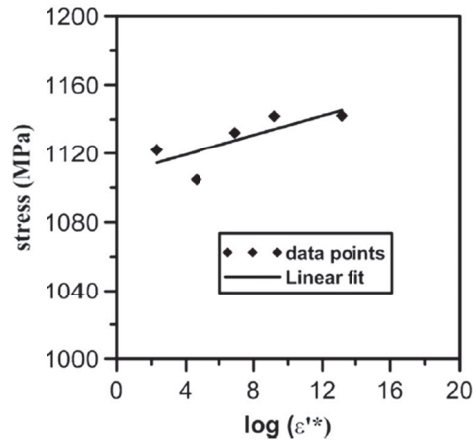


Figure 5: Variation of stress with log of strain rate extracted from [12].

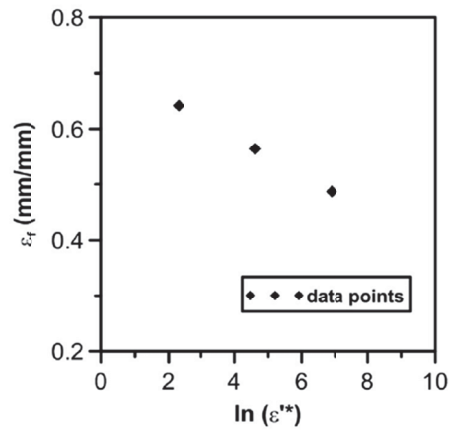


Figure 6: Variation of failure strain with ln of strain rate extracted from [12].

2.4.2.4 Step 4: Effect of temperature

Tensile tests at various temperatures are conducted to obtain the temperature-sensitive m and D_5 values of Equations (30) and (31).

$$\sigma = (\sigma_0 + B\epsilon^n) \left(1 + C \ln \frac{\dot{\epsilon}}{\dot{\epsilon}_0} \right) [1 - (T^*)^m] \quad (30)$$

Both brackets known

$$\epsilon_f = [D_1 + D_2 \exp(D_3 \sigma^*)] [1 + D_4 \ln(\dot{\epsilon}_p^*)] [1 + D_5 T^*] \quad (31)$$

Both brackets known

The JC stress equation is rearranged in such a manner that K corresponds to its non-temperature sensitive components:

$$K = (\sigma_0 + B\epsilon^n) \left(1 + C \ln \frac{\dot{\epsilon}}{\dot{\epsilon}_0} \right) \quad (32)$$

All the necessary constants of this equation have been obtained previously. Applying the above substitution to the original JC equation yields:

$$\sigma_{eq} = K(1 - (T^*)^m) \quad (33)$$

Applying the log function and a few manipulations yields:

$$\log(K - \sigma_{eq}) = m \log(T^*) + \log K \quad (34)$$

Plotting the data from the tensile tests conducted at variable temperature on a log scale should yield results such as the ones in Figure 8. The slope of the linear curve obtained corresponds to the constant m .

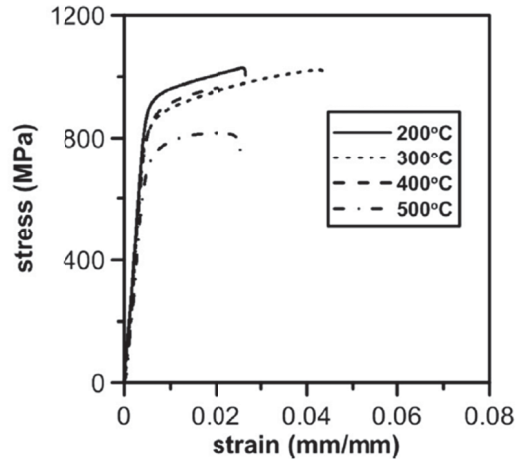


Figure 7: Stress-strain curves as a function of temperature extracted from [12].

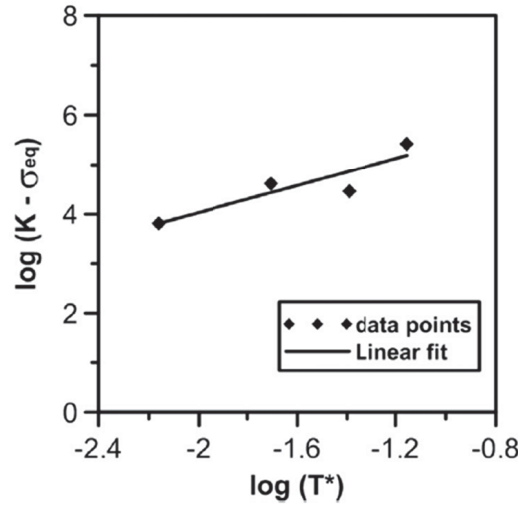


Figure 8: Graph plotted to find temperature constant m extracted from [12].

In order to obtain the final missing value D_5 from the strain equation, failure strain is plotted against the unit-less temperature T^* and a line of best fit is applied.

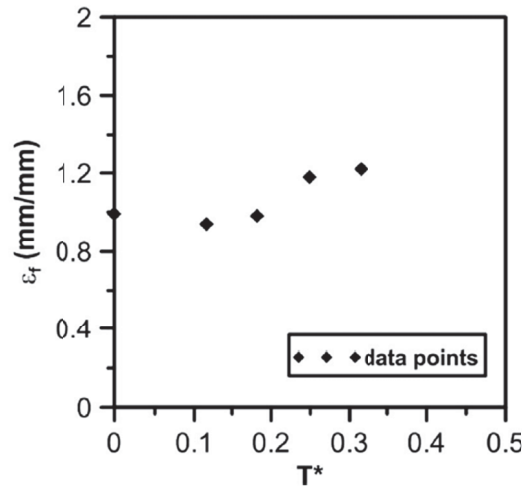


Figure 9: Failure strain vs. dimensionless temperature to find D_5 parameter extracted from [12].

Many authors such as Lesuer et al. [13], Manes et al. [14] and Toussaint and Bouamoul [15] showed that the strain rate sensitivity of Aluminium 6061-T6 can be neglected in certain strain rate range.

2.4.3 Zerilli-Armstrong model

Armstrong and Zerilli [16] found that the dislocation mechanisms of metals varied based on their crystal structures. In Fully Centred Cubic (FCC) metals, dislocations must traverse the barriers of forest dislocations, and the thermal activation area decreases with plastic strain because of the increase in dislocation density. For Body Centred Cubic (BCC) metals, dislocations must overcome Peierls-Nabarro barriers (i.e., Peierls internal stress), such that the thermal activation area is not related with strain. Hence, the yield stress of FCC metals is determined mainly by strain hardening, but that of BCC metals is basically determined by strain rate hardening and temperature softening. Based on these considerations, they proposed the Zerilli-Armstrong (ZA) model with different constitutive forms for FCC and BCC and for Hexagonal Closed Pack (HCP) metals which owns mixed characteristics of the BCC and FCC structures [17]. Aluminium is a FCC metal [18].

However, Voyiadjis and Abed [19] pointed out that the ZA model is not applicable to the deformation of metals under high temperature and that this model does not include the strain rate effect on thermal activation area. Over time, Voyiadjis and Abed [19] and others proposed variations of the ZA model that would attempt to compensate for these shortcomings. However, this model, and its variants are generally suitable for strain rates below 10^4 s^{-1} . Follansbee and Kocks [20] found that the flow stress of Oxygen-Free High Conductivity (OFHC) copper and some other FCC metals increases dramatically when the strain rate exceeds a certain value [17]. Figure 10 presents their experimental results comparing the results of various damage models. It can be observed that for this material, the Gao-Zhang (GZ), Langer-Bouchbinder-Lookman (LBL) and Nemat-Nasser-Li (NNL) models give the best approximation until a strain rate of roughly 10^2 or 10^3 s^{-1} after which the Zerilli-Armstrong becomes the most accurate until the transition zone of OFHC Copper.

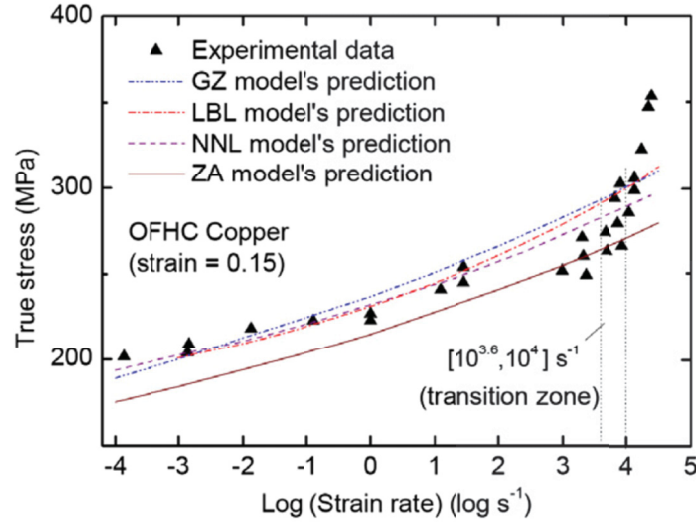


Figure 10: Experimental data and simulation results of samples failing at various strain rates ([17] extracted [20]).

Although a number of models have been proposed based on Dislocation Density Evolution (DDE) to explain this sudden rise, the physics of the dislocation generation at extremely high strain rates are still not very clear according to Gao and Zhang [17].

Zerilli-Armstrong is a rate and temperature sensitive plasticity model which is sometimes preferred in ordnance design calculations [4].

It defines flow stress as:

$$\sigma = C_1 + \left\{ C_2 (\epsilon^p)^{\frac{1}{2}} [e^{[-C_3 + C_4 \ln(\dot{\epsilon}^*)]T}] + C_5 \right\} \left[\frac{\mu(T)}{\mu(293)} \right] \quad (35)$$

It should be stressed that the above equation is specifically for FCC metals, and corresponds to the below BCC metal equation when n is set to zero.

$$\sigma = C_1 + C_2 [e^{[-C_3 + C_4 \ln(\dot{\epsilon}^*)]T}] + [C_5 (\epsilon^p)^n + C_6] \left[\frac{\mu(T)}{\mu(293)} \right] \quad (36)$$

Note:

$$\begin{aligned} \epsilon^p &= \text{effective plastic strain} \\ \dot{\epsilon}^* &= \text{effective plastic strain rate} = \frac{\dot{\epsilon}}{\dot{\epsilon}_0} \end{aligned}$$

Where $\dot{\epsilon}_0$ will equal 1, 1×10^{-3} or 1×10^{-6} if seconds, milliseconds or microseconds are respectively used.

$$\frac{\mu(T)}{\mu(293)} = B_1 + B_2T + B_3T^2 \quad (37)$$

The relationship between heat capacity (specific heat C_p) and Temperature (T) may be characterized by a cubic polynomial equation as follows:

$$C_p = G_1 + G_2T + G_3T^2 + G_4T^3 \quad (38)$$

Where G are constants to be determined. The optional fully viscoplastic formulation will require more computing, but gives improved results [4].

In the LS-DYNA hydrocode, these initial uncoupled constitutive models will very often include some form of failure criterion or criteria. These constitutive models may also be combined to damage models and/or to other failure models such as the *mat_add_erosion* or Generalized Incremental Stress State dependant damage MOdel (GISSMO). These damage/failure models allow to predict fracture, spalling and the formation of shear bands.

2.4.4 Cockcroft-Latham Ductile failure criterion

The Cockcroft-Latham ductile failure criterion is defined in [21].

$$\int_0^{\bar{\epsilon}_f} \sigma_{max} d\bar{\epsilon} = C_1 \quad (39)$$

σ_{max} = Maximum principal stress
 $\bar{\epsilon}$ = equivalent strain

By adjusting the equation, we can obtain:

$$I = \frac{1}{C_1} \int_0^{\bar{\epsilon}_f} \sigma_{max} d\bar{\epsilon} \quad (40)$$

The value I represents the normalized damage value, which varies from 0 to 1. It is calculated at each point of a FE analysis, when a point reaches an I value of 1, it is deleted [4]. More details are provided in the reference [21].

2.4.5 GISSMO—Generalized Incremental Stress State dependent damage Model

The Generalized Incremental Stress State dependant damage MOdel (GISSMO) is represented by the following formula [4]:

$$\Delta D = \frac{n}{\epsilon_f(\eta)} D^{(1-\frac{1}{n})} \Delta \epsilon_p \quad (41)$$

Where:

D is the current damage ($0 < D < 1$, where 0 is an intact element and 1 is a destroyed element) $\Delta \epsilon_p$ is the increment of plastic strain, n is the experimentally determined damage exponent, $\epsilon_f(\eta)$ is the fracture strain as a function of η , η is the triaxiality which is defined as the ratio of hydrostatic (σ_{hyd}) and Von Mises (σ_{vm}) stress.

The GISSMO model has also an instability parameter:

$$\Delta F = \frac{n}{\epsilon_{crit}(\eta)} F^{(1-\frac{1}{n})} \Delta \epsilon_p \quad (42)$$

Where:

ϵ_{crit} is the equivalent plastic strain to instability, it is a function of triaxiality.

When F is equal to zero, the material behaves in an elastic manner, when it is equal to 1, the damage affects the stress in the following manner:

$$\sigma = \tilde{\sigma} \left(1 - \left(\frac{D - D_{crit}}{1 - D_{crit}} \right)^m \right) \quad (43)$$

Where:

D_{crit} is the damage value at the moment F becomes 1 (D_{crit} may be set to zero). m is the “fading exponent” which must be calibrated to experimental results. $\tilde{\sigma}$ is the effective stress.

It can be observed that by setting D_{crit} to zero, and m to one, that the Lemaitre damage model [22] is obtained.

As a reminder, the damage law from Lemaitre [22] takes the form below, and is based on the idea that the effective stress of a plastically deformed material is a function of its true area which consists of both intact material, and failed material.

$$\sigma = \tilde{\sigma}(1 - D) \quad (44)$$

The D value, as before, is the damage variable. Let S be the overall section area, S_D , the destroyed material area and \tilde{S} the effective resisting area:

$$\tilde{S} < S - S_D \quad (45)$$

Then the damage variable D is defined by Equation (45) [22].

$$D = \frac{S - \tilde{S}}{S} \quad (46)$$

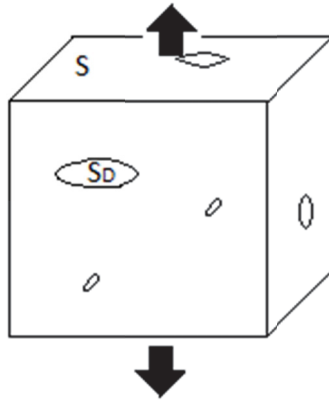


Figure 11: Schematic representation of the damage material area (S_D) and the intact material area (S).

The values of D and F as a function of material states are presented in Table 3.

Table 3: Evolution of instability (F) and damage (D) values during a tensile test.

State	F	D
Elastic Region	0	0
Onset of Plastic Deformation	Begins increasing	0
Onset of necking (Peak Load)	1	Begins increasing
Failure		1

Examples of the use of the GISSMO model can be found in the literature [23, 24, 25, 26].

2.4.6 DIEM—Damage Initiation and Evolution Model

One potential advantage of the Damage Initiation and Evolution Model (DIEM) over GISSMO is that it allows an arbitrary amount of damage initiation and evolution criteria to be implemented. GISSMO, on

the other hand, will only implement a single instability and single fracture curve to define material behavior [24]. An example of comparison of these two models is presented in [25, 27].

In the DIEM model, damage initiation is a variable that will evolve until it reaches the critical value of 1, after which, damage evolution begins.

The ductile damage initiation indicator is defined by:

$$\omega_D = \frac{\dot{\epsilon}^p}{\epsilon_D^p} \quad (47)$$

Where ϵ_D^p is a function of triaxiality and strain rate and represents the plastic strain at onset of damage.

Upon ω_D reaching 1, the damage variable D affects the stresses. In DIEM, failure takes place when $D = 0.99$, after which, the element is assumed to have no load-carrying capacity. Damage evolution is expressed as:

$$D = \frac{\dot{u}^p}{\frac{\delta u_f^p}{\delta D}} \quad (48)$$

Where u^p and u_f^p are the plastic displacement and the plastic displacement at failure, respectively. On the surface, using Lemaître's equation rather than equation (52) makes it appear that some freedom in the calibration of results is being sacrificed. However, the plastic displacement at failure may be programmed as a function of triaxiality and damage. The end result is something resembling the damage fading exponent in GISSMO.

The evolution of the plastic displacement is defined as:

$$\dot{u}^p = \begin{cases} 0 & \omega_D < 1 \\ l\dot{\epsilon}^p & \omega_D > 1 \end{cases} \quad (49)$$

Where l is the characteristic length of the element. This parameter is introduced as a way to correct the energy dissipation error due to mesh dependency [24].

DIEM will also allow the definition of a shear damage initiation indicator. The plastic strain at onset of damage is now a function of the shear stress function, θ , instead of triaxiality.

$$\theta = \frac{2(\sigma_{eq} + k_s p)}{\sigma_{major} - \sigma_{minor}} \quad (50)$$

However, this appears redundant because, by definition, triaxiality considers all loading conditions, including shear.

For shell elements, DIEM allows for the definition of two instability criteria: Forming Limit Diagram (FLD) and Mûschenborn and Sonne Forming Limit Diagram (MSFLD). In these models, plastic strain at onset of damage is a function of the in-plane deviatoric stress ratio α :

$$\alpha = \frac{S_{minor}}{S_{major}} \quad (51)$$

Andrade et al. [24] compared material failure prediction using DIEM and GISSMO, and could not see an advantage to using multiple DIEM failure criteria over the single one in GISSMO in their experiments. Good calibration of parameters in GISSMO using the plane stress assumption for triaxiality was sufficient. It should be noted that this conclusion was drawn from their experiments and simulations which only involved thin specimens. Furthermore, some GISSMO parameters need to be fine-tuned to element size, whereas this is explicitly done with DIEM in Equation (53). Therefore, in this regard, DIEM may be preferred over GISSMO, but as mentioned before, fine calibration of parameters is the most important aspect of developing a good computer simulation, and both models will give a good representation of actual material behavior. Figure 12 presents the simulations and experiments results extracted from [25].

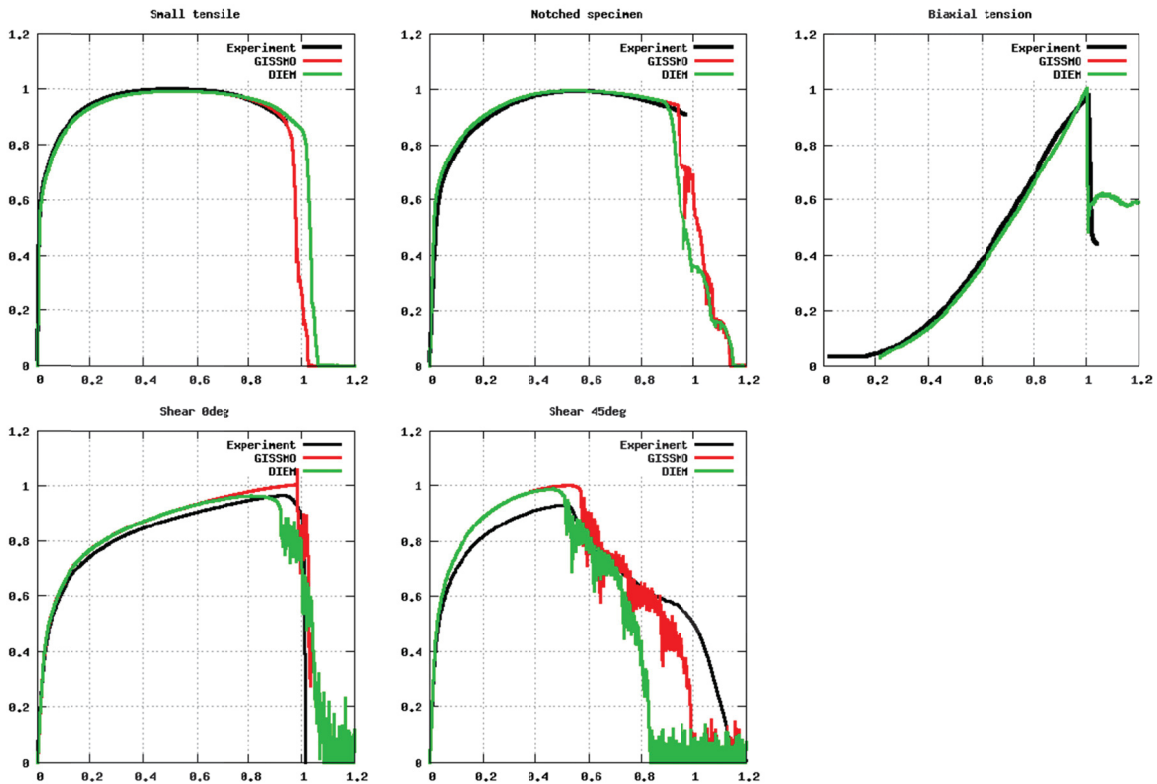


Figure 12: Andrade et al.'s findings showing that a well-calibrated GISSMO model is as effective as DIEM, extracted from [25].

3 Summary of Giglio et al. experimentation [2]

Giglio et al. [2] performed a complete calibration of the Al 6061-T6 using the Bao-Wierzbicki [28] approach as the main framework. Experimental tests were performed in pure torsion, biaxial torsion-traction and torsion-compression in quasi-static. A summary of the tests are provided in Table 4. In this reference, the simulations reproduced these experiments and were performed using the ABAQUS software. The main difference between the Johnson-cook failure model and the Bao and Wierzbicki is that the latest defined the fracture locus, using different equations to cover a wide range of stress triaxiality that are usually only covered partially in the literature, i.e. for a specific test. According to [2], the stress triaxiality range is fairly large in ballistic impact simulations.

Monoaxial tensile tests with smooth round and two different notched round specimens have been carried out. Also, multiaxial tests were performed, in pure torsion and mixed tests in torsion/tension and torsion/compression. Finally, the height to diameter ratios (h/D) was changed for cylindrical specimens. All these tests allowed covering the range of stress triaxiality from $-1/3$ to 0.4. Monoaxial tests were performed for high stress triaxialities (> 0.4), mono and multiaxial tests for low stress triaxiality ($0 \leq \eta \leq 0.4$) and also, monoaxial upsetting tests were also conducted. Table 4 provides a summary of these tests. An electro-mechanical MTS Alliance RF150 machine was used for the mono-axial tests while a servo-hydraulic multi axial machine MTS 809 was used for the multi-axial tests. Figure 13 provides the drawings of the different specimens.

Table 4: Summary Giglio et al. experiments results [2].

Type of load		Type of specimen	Superimposed constant load
Monoaxial	Tension	Round smooth	N/A
Monoaxial	Tension	Round notched (Radius 12 mm)	N/A
Monoaxial	Tension	Round notched (Radius 5 mm)	N/A
Monoaxial	Torsion	Round smooth	N/A
Multiaxial	Torsion	Round smooth	Traction (4kN)
Multiaxial	Torsion	Round smooth	Traction (8kN)
Multiaxial	Torsion	Round smooth	Compression (12kN)
Monoaxial	Compression	Cylinder	N/A

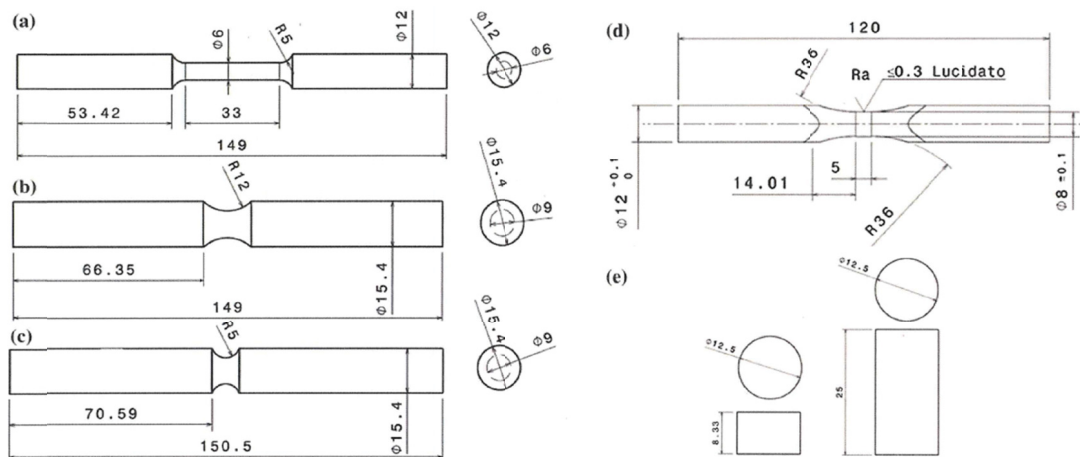


Figure 13: a) Round smooth specimen b) Round notched specimen (notch radius 12 mm) c) Round notched specimen (notch radius 5 mm) d) Pure tension and multiaxial specimen e) Upsetting specimen, extracted from [2].

4 Numerical simulations

The objective of the following section is to reproduce the experimental results on Al 6061-T6 extracted from Giglio et al. research [2] using different constitutive models such as the *mat_plastic_kinematic*, *mat_johnson_cook* and *Generalized Incremental Stress State dependant damage MOdel (GISSMO)*. Also, to investigate the effects of several parameters on the true stress-strain curves. The first simulation to be performed will allow identifying the parameters that will be used to reproduce adequately the simulation of a simple tensile test made from Al 6061-T6 material. Then, using the parameters obtained from this simulation, the second step will be to perform simulations of experimental tests that will allow evaluating the fracture locus at different triaxialities.

The geometry of the tensile specimen, shown in Figure 14, was generated following the dimensions provided in [2]. The geometry of a 2D axisymmetric model was meshed with 0.5 mm elements size and in order to reduce calculation time, the length of both ends was shortened.

In order to replicate the experimental conditions, strain measurements were taken from a virtual 25 mm long extensometer,¹ and stress readings were taken as the average between the core of the sample and the outside along the critical cross-section.² Nodes were fixed on one end and a velocity of 10 mm/s was applied to the nodes at the other end.

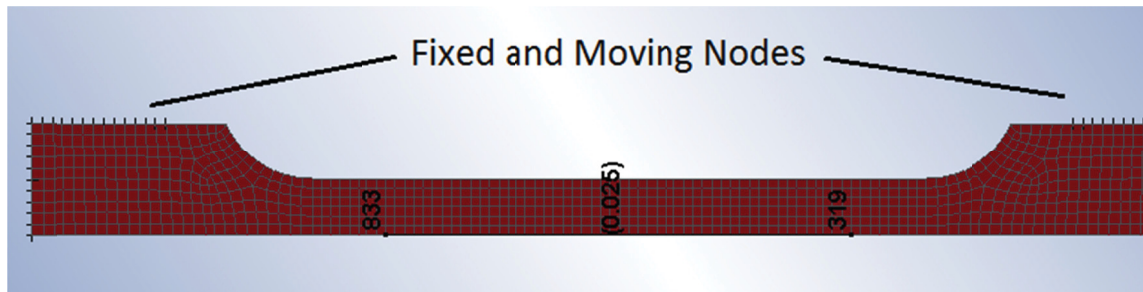


Figure 14: 2D axisymmetric model of a tensile sample.

4.1 Simulations using the *mat_plastic_kinematic* constitutive model

The first series of simulations was run with LS-DYNA hydrocode [1] using the material model *mat_plastic_kinematic*. The material constants required for *mat_plastic_kinematic* that were initially used are presented in the following table.

¹ Initially, extensometer readings were taken at the core of the sample, but this was corrected to the outer surface in later simulations. The correct node numbers are 367 and 881.

² While taking the average stress along a cross section would, at first glance, make more sense in an attempt at replicating the readings of a real tensile testing machine, it was later discovered that the outside stress matched results much more closely. According to Kut [29], the fracture strain should be determined in the lateral zone of a plane specimen during a tensile test as the state of stress in this area is closer to uniaxial tension.

Table 5: *Al 6061-T6 constitutive model constants.*

Proerties	Symbols	Values	Units	Sources
Density	RO	2700	kg/m ³	[2]
Young's Modulus	E	70	GPa	[2]
Poisson's Ratio	PR	0.33		[2]
Yield Stress	SIGY	270	MPa	[2]
Tangent Modulus	ETAN	1.33	GPa	[30]
Strain Rate Parameter C	SRC	6500	s-1	[31]
Strain Rate Parameter P	SRP	4		[31]
Failure Strain	FS	0.11535 ⁴		[2]

The literature did not provide the failure strain explicitly, therefore, the failure strain was estimated by measuring a force/displacement curve; assuming the initial length was the extensometer length. The failure strain extracted from Giglio et al. tensile test data [2] agrees with data from ASM International [7] for a tensile rod (0.108+), but is significantly lower than Dorbane et al. [32] failure strain (0.1806). There was various values obtained when comparing data from other sources but as explained previously, the failure strain is mesh dependant.

The stress-strain curves below were produced by replicating the testing conditions of Giglio et al. experiments [2]. The stress is the average Y-stress of the cross-section where initial failure occurs, where the average taken between the Y-stress at the core of the sample, and on the outer perimeter. The displacement is recorded using a virtual extensometer with a mounting point 12.5 mm above and below the centerline. The difference of Y-displacement between the tensile sample core and circumference is considered negligible.

4.1.1 First trials: Varying the hardening parameter

The first trials used a tangent modulus (ETAN) of 1.33 GPa obtained from the work of Kwon and Thompson [30] and a hardening parameter β (Beta) of 0 and 1. The values of 0 and 1 respectively correspond to kinematic hardening and isotropic hardening has explained in the LS-DYNA manual [4]. An additional intermediate value of 0.13 was also tested in this work. Isotropic hardening ($\beta = 1$) is when the yield surface retains the same form, but expands with increasing stress [33].

In order to model the Bauschinger effect, where a hardening in tension will lead to a softening in subsequent compression, the kinematic hardening rule ($\beta = 0$) can be used. Here, the yield surface will remain the same shape and size, but will translate in stress space [33].

³ This tangent was too steep and did not replicate the experimental results. Ultimately, 874 MPa was used with greater success.

⁴ The failure strains obtained from literature had very important variations.

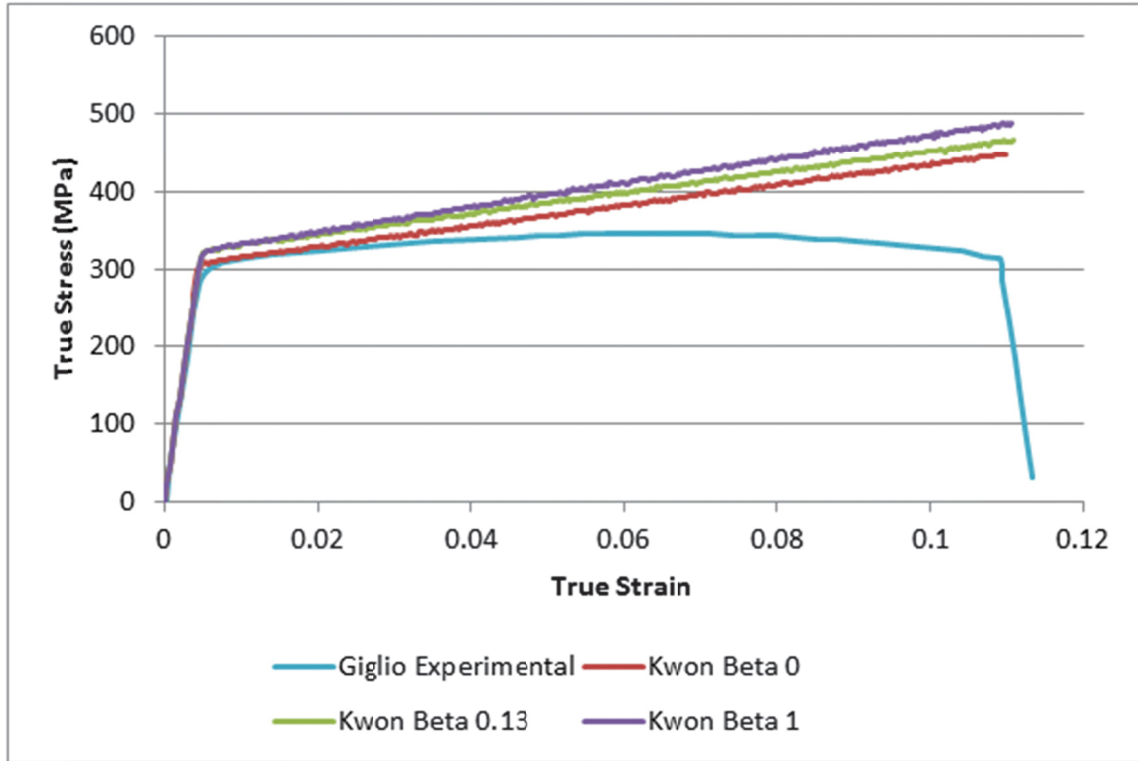


Figure 15: Effect of the Beta Parameter (0, 0.13 and 1) using Giglio et al. experiments [2].

Notice that in Figure 15, the true stress-strain curve of Giglio et al. [2] is only valid until necking point. From Figure 15, it may be observed that having a non-zero Beta value increases the beginning of the plastic stress tangent modulus. Since the yield stress used in the current simulations was the one obtained in Giglio et al. experiments [2], the yield stress will not be modified in LS-DYNA, but instead, the beta value of 0 will be used.

4.1.2 Second trials: Varying the tangent modulus

The tangent modulus were obtained from Kwon and Thompson [30] and Berger-Pelletier [34] which respectively proposed 1.33 GPa [30] and 645.7 MPa [33]. In addition, a third one was calculated by obtaining the ETAN and E_h values from the true stress and true strain from Giglio et al. [2]. The ETAN and E_h values vary at each point, therefore, the variation was calculated between each, and the average value of the tangent was obtained for the region of plastic strain where variation was relatively small (between -69 and -53 MPa per point in this research). The value obtained for the tangent modulus was set to 893.74 MPa in this section.

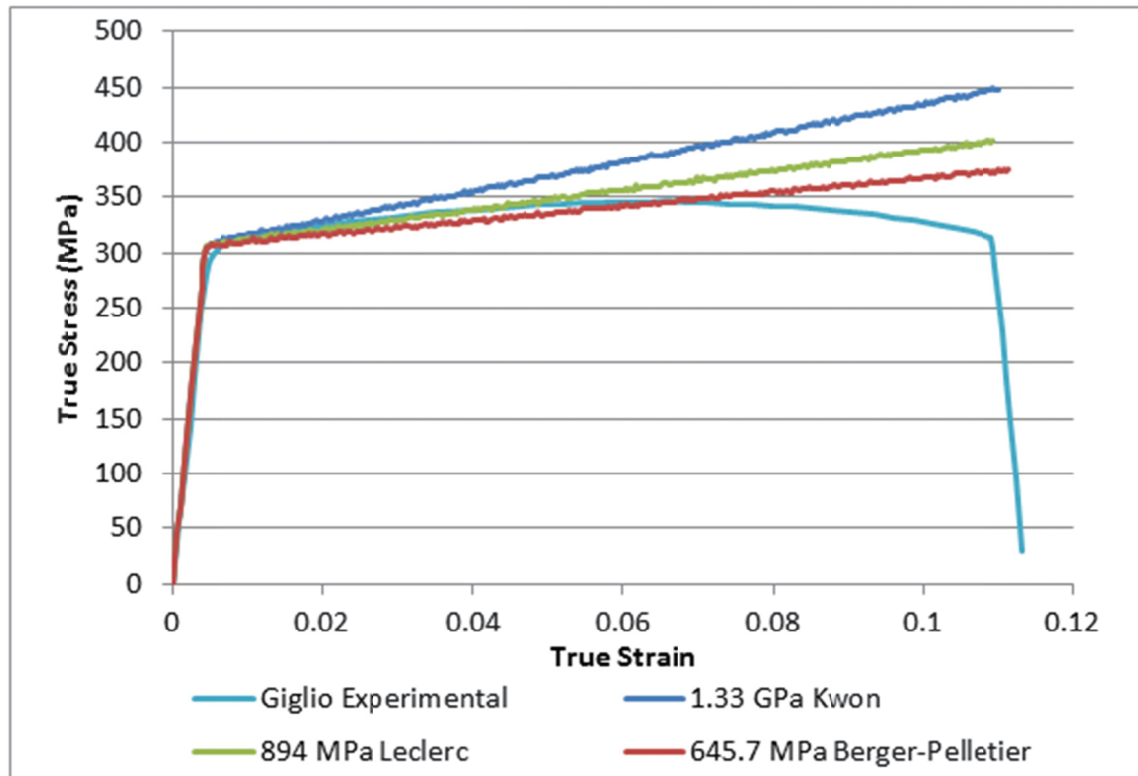


Figure 16: Calibration of tangent modulus to Giglio experimental results.

Again, notice that in Figure 16, the true stress-strain curve of Giglio et al. [2] is only valid until necking point. Figure 16 presents the engineering stress strain curve using Giglio et al. [2], Kwon and Thompson [30], Berger-Pelletier [34] and a mean value. At the beginning of the plastic curve, the value of 894 MPa slope seems to provide an adequate correlation with Giglio's et al. experimental data [2]. Others true-stress/strain curves were consulted from literature [2, 7, 35, 36] and are presented in Figure 17.

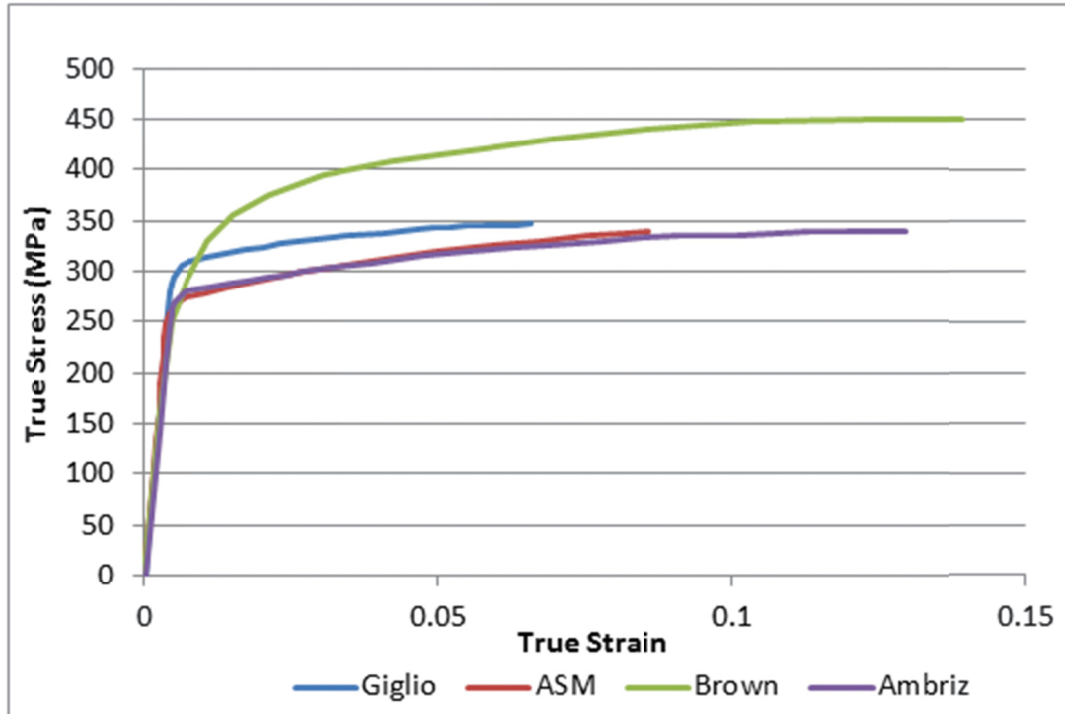


Figure 17: Tensile test results from literature [2, 7, 35, 36].

The Young's modulus of all four sources is similar, but there is a wide variation when comparing the plastic curves, Brown et al. [35] curve has a significantly higher failure stress than the three other sources. The three other sources have very similar failure stresses, but have a wide variation in the failure strain.

All the parameters used were tailor-made for this specific situation i.e. a quasi-static tensile test at room temperature that only goes over a small positive range of triaxialities.

The next section presents the Johnson-Cook constitutive model. This material model can be used to include the effects of strain rates and temperature. The Aluminum alloy 7075 is an example of material where the strain rate and temperature have an influence on its mechanical properties [37].

4.2 Simulations with *mat_johnson_cook* constitutive model

The Johnson-Cook model is a well-accepted constitutive model that is widely used in the literature; it was therefore possible to find parameters in the literature [2, 13]. The *mat_johnson_cook* model considers the effects of strain rate, strain hardening, and temperature effects. When combined with other appropriate models, the combined models can also consider damage accumulation.

In this section, the simulations were performed using the parameters provided in Table 6.

Table 6: Johnson-Cook constitutive model parameters.

Properties	Symbols	Values	Units	Sources
Density	RO	2700	kg/m ³	[2]
Shear Modulus	G	26	GPa	[2]
Young's Modulus	E	70	GPa	[2]
Poisson's Ratio	PR	0.33		[2]
Yield Stress	A	270	MPa	[2]
Hardening factor	B	165.5	MPa	[2]
Hardening exponent	N	0.222		[2]
Strain Rate Factor	C	0.011		[2]
Temperature Exponent	m	0 ^a		[2]
Melting Temperature	TM	925 ^b	K	[13]
Reference Temperature	TR	294 ^b	K	[2]
Specific Heat	C _p	890	J/kg·K	[2]

^a Assumed negligible.

^b Ignored because m = 0.

When damage was included, the values presented in Table 7 were used in the simulations; otherwise, they were all set to zero.

Table 7: Johnson-Cook damage model parameters.

Damage Parameters	Symbols	Values	Source
Triaxiality Constant	D ₁	-0.77	[13]
Triaxiality Factor	D ₂	1.45	[13]
Triaxiality Exponential Factor	D ₃	-0.47	[13]
Strain Rate Factor	D ₄	0.011	[2] ^c [13]
Temperature Factor	D ₅	1.6	[13]

^cGiglio et al. (2014) cited the paper from Lesuer et al. (2001) for these numbers, but the D₄ values differ. Lesuer et al. (2001) published "0.0" while Giglio cited "0.011".

4.2.1 First Trials: Evaluating effect of damage and erosion activation and desactivation

For these simulations of tensile test, the damage and erosion settings were set in the *mat_johnson_cook* by changing the EROD parameter from 1 to 0, and making the D values equal to 0, or defining their values as found in the literature (presented in Table 7).

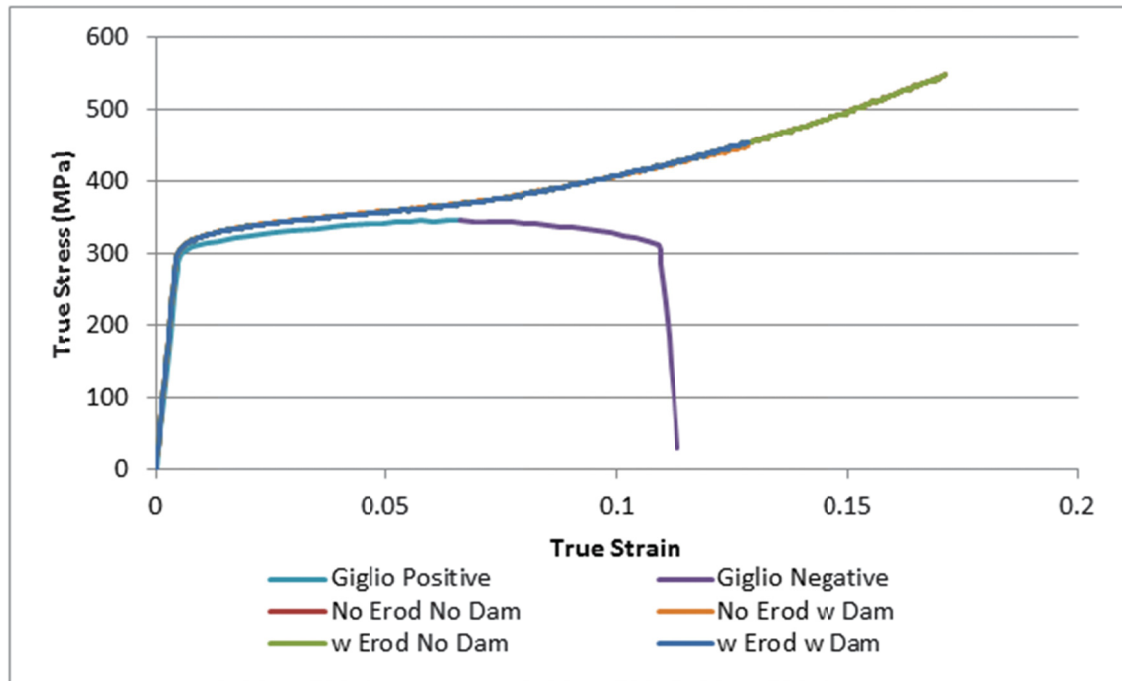


Figure 18: *Effect of damage and erosion settings in a tensile test simulation.*

Upon closer observation of Figure 18, the “No Erod No Dam” curve does not seem to appear. This is actually because the “w Erod No Dam” curve overlaps it entirely. Both the curves with damage give very similar data, but failure occurs very differently. While the simulation with erosion and with damage ends with element deletion, the simulation without erosion ends in over-strained elements that ultimately cause the simulation to crash. It appears that the activation of damage creates the conditions necessary to fail at a certain strain, but only the activation of erosion will actually make it possible to delete elements. It should be noted that EFMIN was set to zero for all simulations, and therefore, LS-DYNA was relying solely on the D parameters to determine when to delete elements. Under normal circumstances, LS-DYNA compares EFMIN with the D parameter equation, and chooses the one with the highest value of the two to trigger element deletion. When both EFMIN and the D parameters are set to zero, it seems that they are ignored and elements are never deleted, and the simulation only terminates if strain becomes excessively high, triggering LS-DYNA to detect negative volumes and to crash eventually.

The most striking observation is that none of the simulations failed anywhere near the predicted failure strain. Due to the fact that the D parameters are solely responsible for triggering element failure, and these values were used successfully by various researchers, it is assumed that Giglio’s experimental data [2], as thought, shows very premature failure of the sample. The failure strain obtained using the current JC parameters closely follows Brown et al. [35] and Ambriz and Jaramillo [36]. The true stress at failure is very close to Brown et al. [35] as well. However, results showed much higher stresses than any other curves obtained from literature.

4.2.2 Second trials: Influence of alternative D_4 parameter

Simulations were run to compare using Giglio et al. [2] the D_4 parameter cited of 0.011, and Lesuer et al. [13] original 0.0 value. The D_4 parameter corresponds to a strain rate parameter, therefore, since it is very small, the small difference it is not expected to be very significant. Figure 19 shows the true stress true strain curve and compares $D = 0$ and $D = 0.011$.

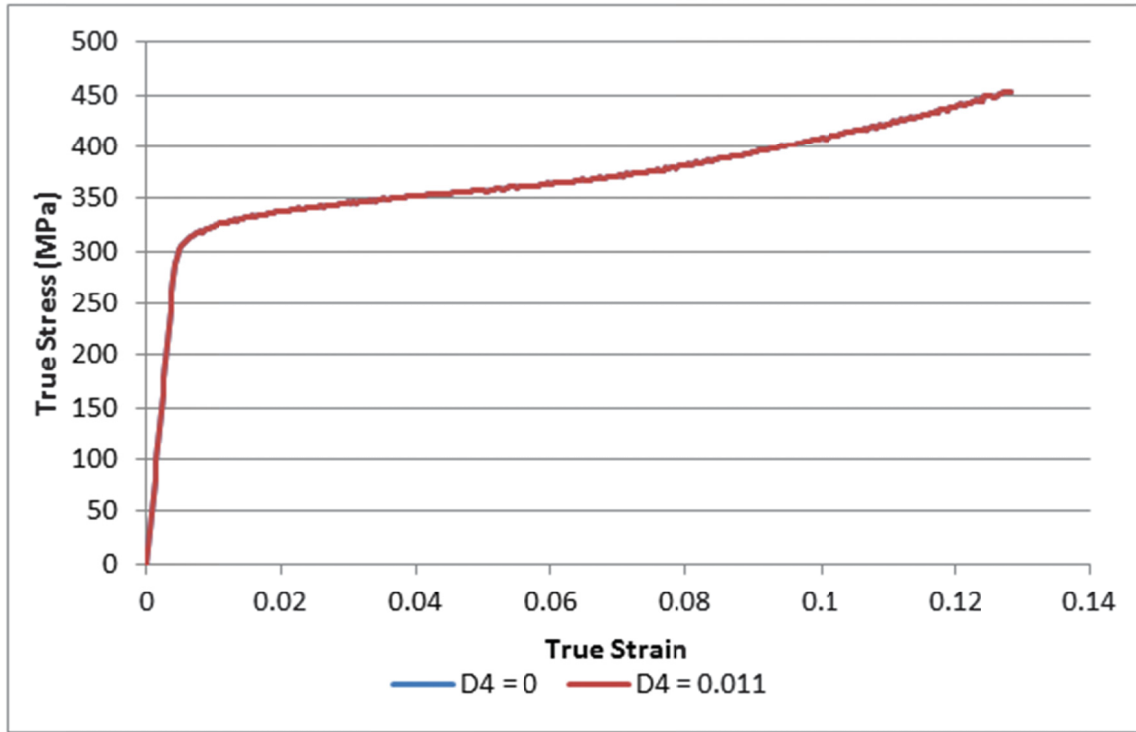


Figure 19: Comparison of simulation results of a tensile test using two D_4 values from literature.

According to the results obtained, the small variation in the D_4 can be neglected in quasi-static. However, if simulations would be done at high strain rates, verification should be done to verify its influence.

4.2.3 Third trials: Adding a pressure cut-off value

The Pressure Cut-off (PC) value (as presented in the LS-DYNA manual [4]) value chosen was 326.41 MPa since this is the peak stress encountered in Giglio et al. tensile test [2]. PC simply refers to the “failure stress or pressure cut off.” This value must be kept negative, otherwise, the simulation will run, and the tensile sample will deform primarily outward in the x-direction without producing any detectable stresses anywhere. When a negative value was used in this research, the simulation initiated correctly, but strain became excessive and was concentrated below the top notch. Further deformation resulted in very strong rippling of the mesh along the thin section between the two notch radii.

Neither test using a PC of ± 326.41 MPa produced any reliable information in these simulations. For further simulations, the Pressure Cut-Off will be kept at 0 as in the previous sections.

4.2.4 Fourth Trials: Effects of EFMIN variation

The strain at fracture corresponds to the maximum between the calculated strain and the EFMIN parameter [4].

$$\varepsilon^f = \max \left(\left[D_1 + D_2^{D_3 \sigma^*} \right] [1 + D_4 \ln \dot{\varepsilon}^*] [1 + D_5 T^*], EFMIN \right) \quad (52)$$

Where σ^* is the ratio of pressure divided by the effective stress:

$$\sigma^* = \frac{p}{\sigma_{eff}} \quad (53)$$

Figure 20 presents the true stress strain curve obtained when varying the parameter EFMIN: 0, 0.05, 0.1, 0.5 and 1.

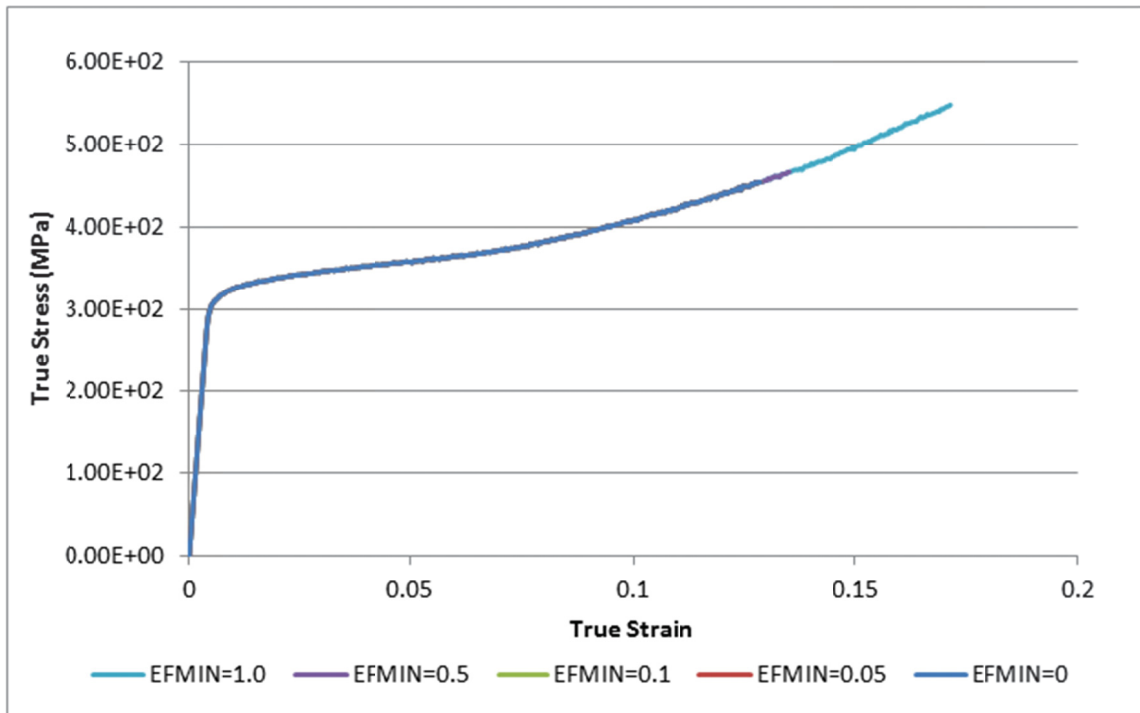


Figure 20: Effect of varying EFMIN on simulation results.

For the values tested, EFMIN had no effect until 0.5. At 0.5, failure was delayed slightly, and at 1, no failure occurred during the 0.5 s simulation. Besides the failure strain, material behavior was identical between all simulations. Therefore, it can be concluded that EFMIN becomes probably larger than the one calculated when it is set around 0.5 and higher.

4.3 Simulations with *mat_johnson_cook* and GISSMO (*mat_add_erosion*)

In his work, Giglio et al. [2] followed the Bao-Wierzbicki approach in which the Johnson-Cook constitutive model was combined to a fracture locus that considers damage evolution and effective plastic strain at failure at various triaxialities. This final model seems to provide very accurate results; therefore, special attention would be taken at this stage to evaluate the validity of certain assumptions made in the previous simulations in order to closely match Giglio's experimental results [2].

4.3.1 First trials: *mat_simplified_johnson_cook* true-stress/strain curves evaluated at different places along critical cross section

The first of these assumptions to be tested would be the one where the stress used by Giglio et al. [2] in his simulations and read-out by his tensile test apparatus correspond to the average stress over the critical cross-section of the tensile sample. Figure 21 presents a comparison between the stress-strain curves obtained by using stress measured at the core of the sample, or on the outer surface, or by doing an average of both values.

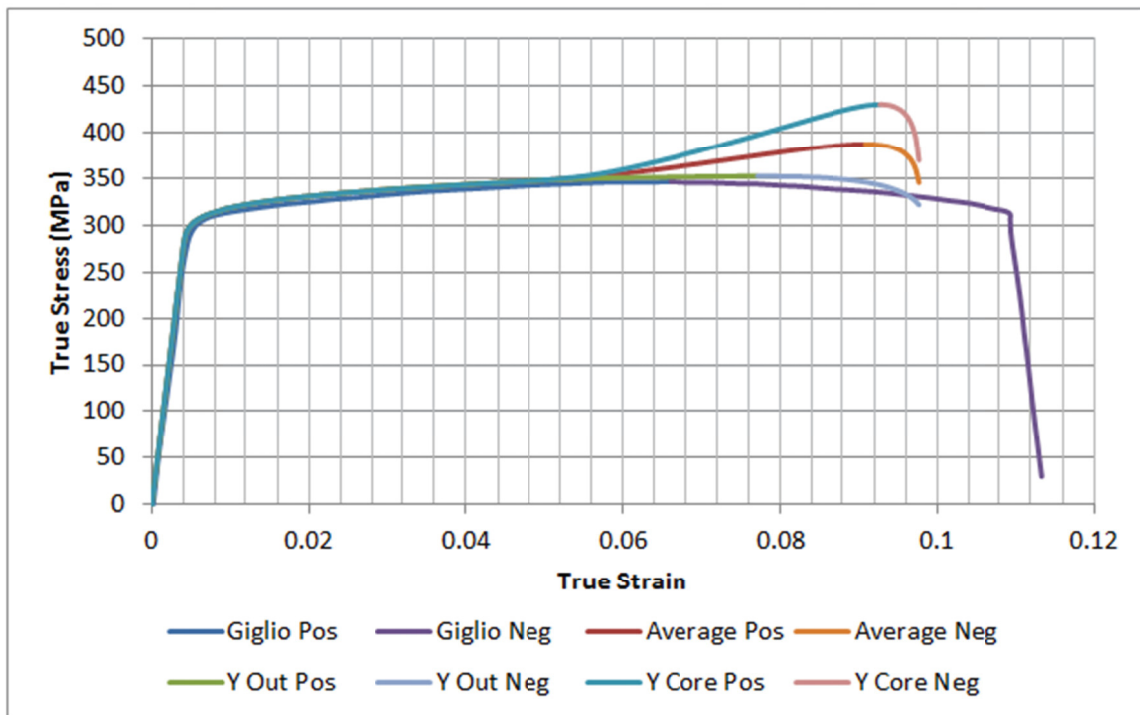


Figure 21: Comparison of the stress-strain curves obtained by using stress measured at the core of the sample, at on the outer surface, and by doing an average of both.

The negative slopes of each curve were printed in separate colours in order to highlight the positive section that would otherwise be the only one present in a genuine true stress/strain curve. The negative portions were preserved for reference.

It becomes clear that although Giglio's parameter values were used, the failure strain is too low, and the stress on the outside of the tensile sample mesh is the most accurate. This goes against the assumption that the physical tensile test machine reads out an average force or stress value. Alternatively, this may imply that Giglio's simulations were all calibrated based on the outside stress. Therefore, the simulation data will be measured using the outside stress from now on.

4.3.2 Second trials: Comparison of damage and Johnson-Cook type settings

In his study, Giglio considered temperature and strain-rate effects to be negligible; therefore, it would be possible to use the *mat_simplified_johnson_cook* instead of the *mat_johnson_cook* constitutive model in this study. The use of the simplified model reduces calculation time, and also allows to verify if the damage parameters (D_1 , D_2 , etc) are set to zero in the JC model would enter into conflict with the presence of the damage criteria of GISSMO. In addition, the influence of the GISSMO damage type on the final results was also tested. Damage type 0 allows damage to be accumulated, but there is no coupling to flow stress, and there is no failure. Damage type 1 allows damage to be accumulated, and triggers element failure at $D = 1$. Damage and flow stress can be coupled based on other parameters with D set to 1.

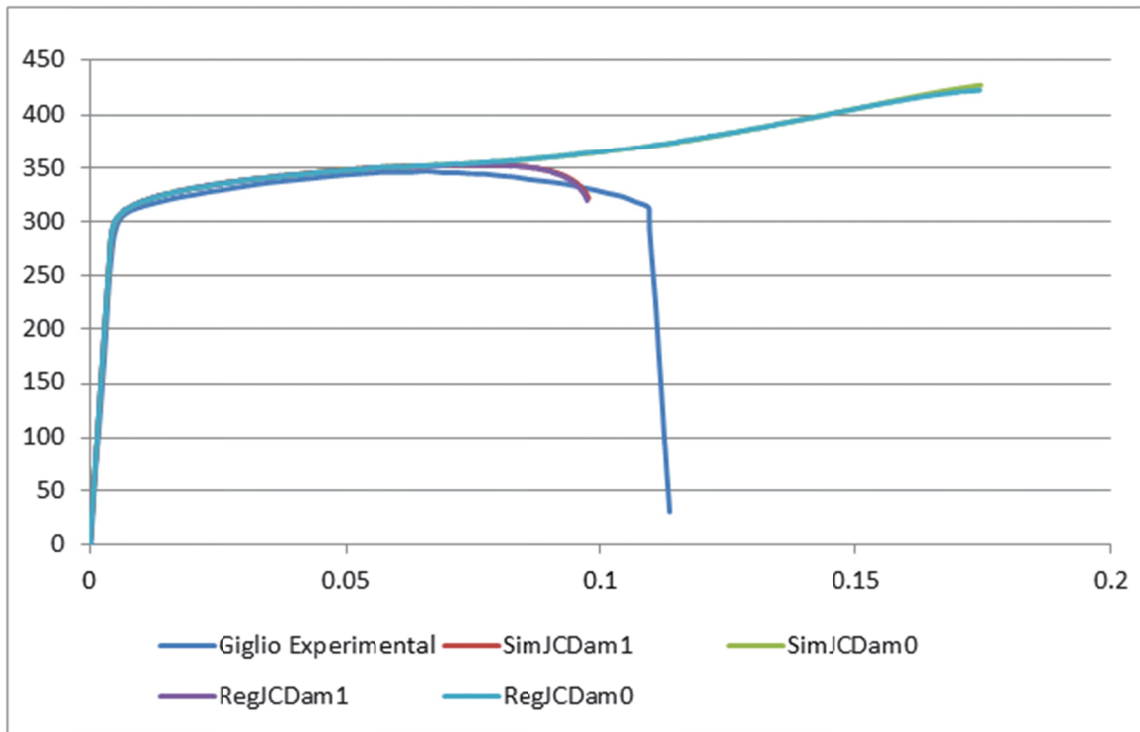


Figure 22: Comparison the *mat_simplified_johnson_cook* model with the *mat_johnson_cook* in conjunction with damage activation or deactivation.

From the above results, it is apparent that using the *mat_simplified_johnson_cook* model is almost equivalent to using the JC model with the additional parameters set to zero, and that the presence of these additional parameters do not interact with the use of the GISSMO model. For further simulations, *mat_simplified_johnson_cook* will be used with the GISSMO damage model set to 1.

4.3.3 Third trials: Adjusting the triaxiality failure curve to obtain the correct failure stress in tension

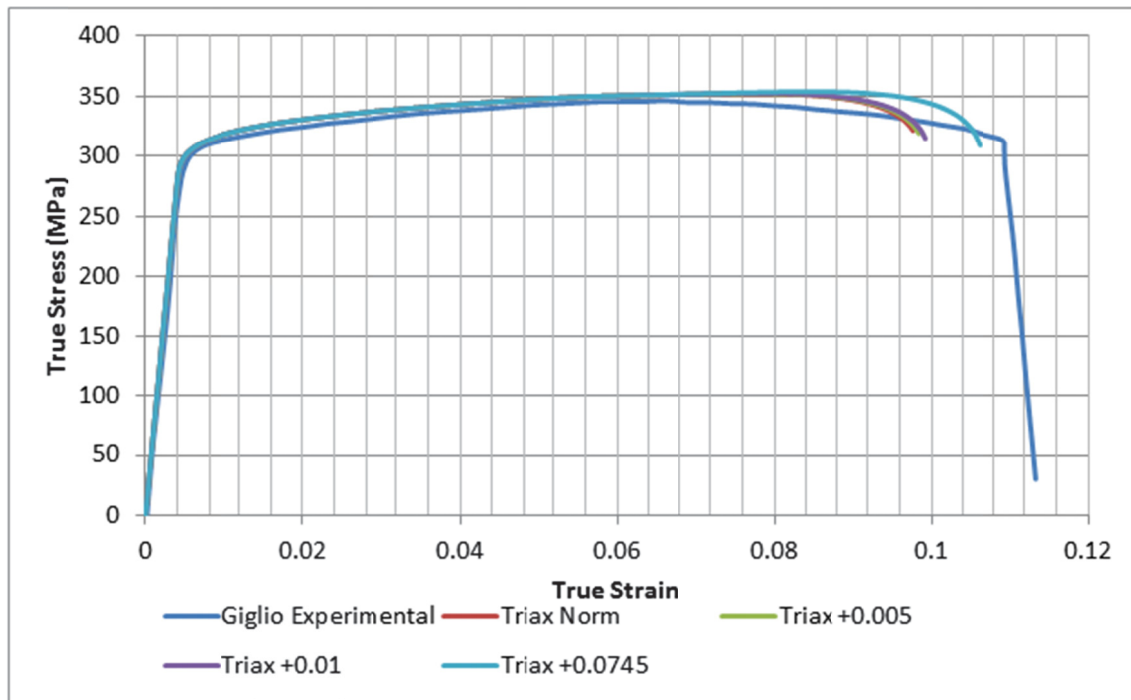


Figure 23: Effect of varying the y-offset of the effective plastic failure strain vs. triaxiality curve.

In order to match the failure strain, and possibly the curvature of the true stress-strain curve in the necking region, the effective plastic strain to failure vs. triaxiality curve was offset and increase in the positive y direction.

In addition to the effective plastic strain to failure vs. triaxiality curve, GISSMO also accepts the input of a critical effective plastic strain vs. triaxiality curve. The critical effective plastic strain is the strain at which necking begins to occur. In all of the above situations, no critical effective plastic strain curve was used because none were available. However, an attempt was made to extract some of this information indirectly. The critical strain simulations are discussed in the “fifth trials.”

Further simulations will keep the +0.0745 offset curve. The failure strain was not calibrated in this step because more parameters will be varied in this JC model. Once the effect of these parameters will be observed, triaxiality curve offset may be reviewed.

4.3.4 Fourth trials: Verifying virtual extensometer assumptions

Early in the simulations, an accurate method of finding experimental strain was found. That is, strain was measured using a virtual extensometer the same size as Giglio’s [2]. The strain data matched very well, and, it was assumed that the Y-displacement did not vary significantly across the cross-sections at which the extensometer ends were located. This older conclusion was made by comparing the absolute difference between data points, which was consistently very small. The validity of this assumption was also reinforced at the time by the simplicity of *mat_plastic_kinematic* which didn’t allow for necking to

occur, and resulted in failure occurring very suddenly across an entire cross section. But, as the simulations became more accurate, and fine tuning became more dependent on the behavior of a sample during the final hundredths and thousandths of a strain, this assumption needed to be closely re-examined. Therefore, the following figure presents the comparison of the Y-displacement surface and core data were obtained from a *mat_simplified_johnson_cook* simulation with GISSMO damage type 1, a triaxiality curve offset of +0.0745, and a fixed critical strain of 0.01.

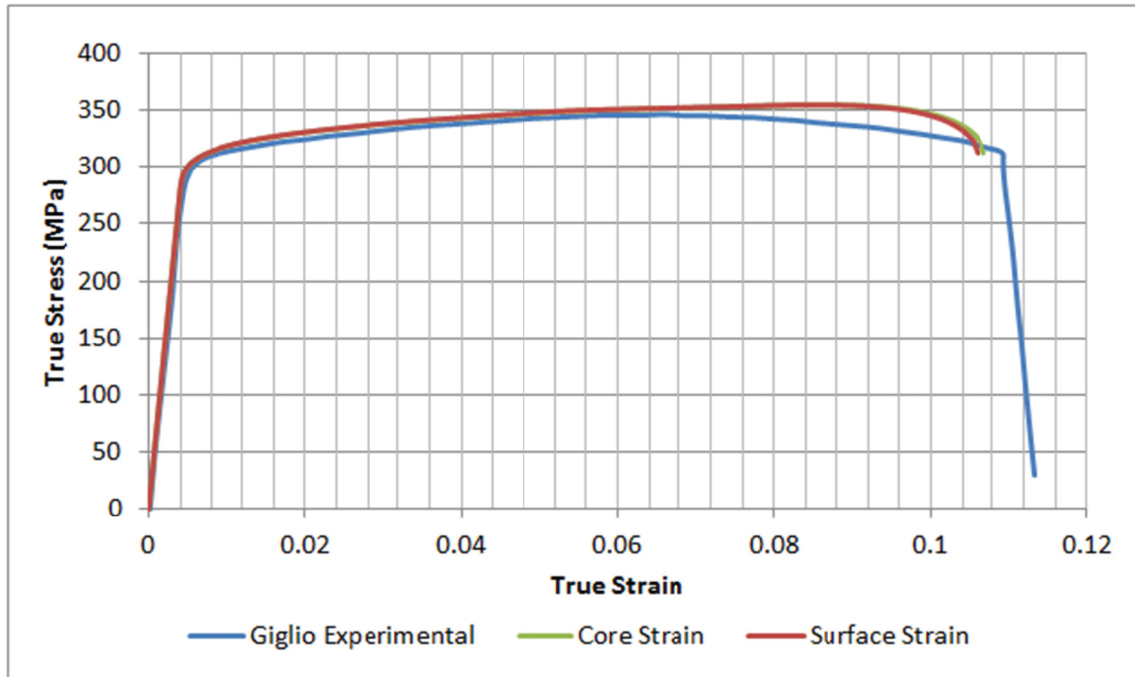


Figure 24: Effect of strain-reading location on stress-strain curve.

The failure strain, when read from the core, is roughly 0.107 compared to 0.106 at the surface, representing nearly a 1% difference. While small, it is understood for the reasons listed above that using the outside displacement reading will be used.

4.3.5 Fifth trials: Verifying virtual extensometer assumptions

In order to adjust the necking region of the stress-strain curve, one hypothesis was to incorporate a partial critical effective plastic strain vs. triaxiality curve extracted from Giglio's data. This was accomplished by taking the displacements at the peak force of each graph in Giglio's report, converting these into true strain and true stress respectively, and obtaining the corresponding effective plastic strains. Only the data points of the critical effective plastic strain vs. triaxiality curve corresponding to tensile tests could be extracted because one of the force vs. displacement graphs was missing from Giglio's study [2], and no vertical displacement data were available for the tests that combined torsion with tension or compression. After generating the curve from the data points available, it was decided to run simulations using it, followed by tests at fixed critical strains to see their effect.

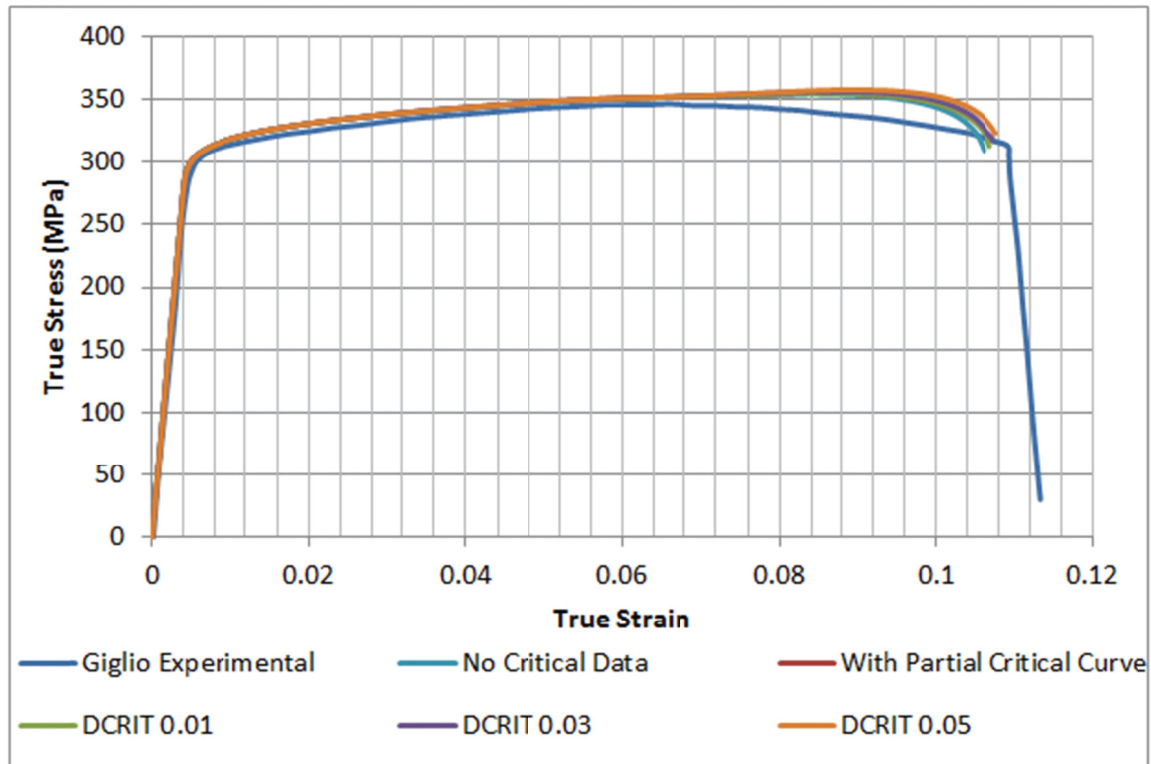


Figure 25: *Effect of critical strain parameters (DCRIT).*

As can be seen in Figure 25, increasing the DCRIT value increases the failure stresses and strains. It should also be noted that the DCRIT = 0.01 and 0.03 curves almost exactly match the curve that was generated using the partial critical strain vs. triaxiality curve. Future simulations will keep the partial curve.

4.3.6 Sixth trials: Adjusting the size regulation factor

An important factor to consider in simulations with high deformation is the effect of changing the element size. This is illustrated in Haufe's work [38] where the effect of the mesh element sizes on the results are presented.

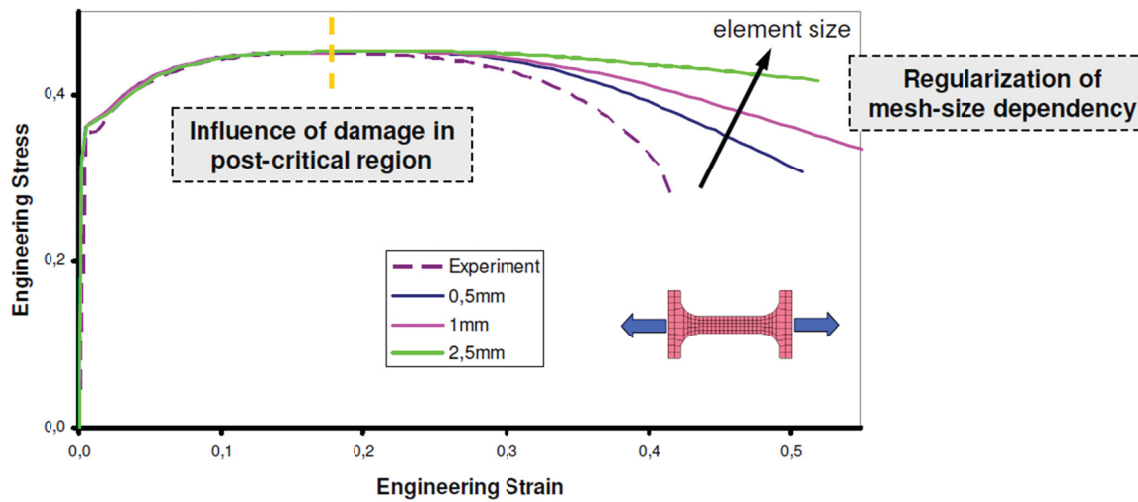


Figure 26: Effect of element size on the engineering stress strain results from Haufe et al. [39].

As presented in Figure 27 extracted from Effelsberg et al. [24], it is possible to calibrate the scaling curve and to obtain very accurate results even when using coarse meshes.

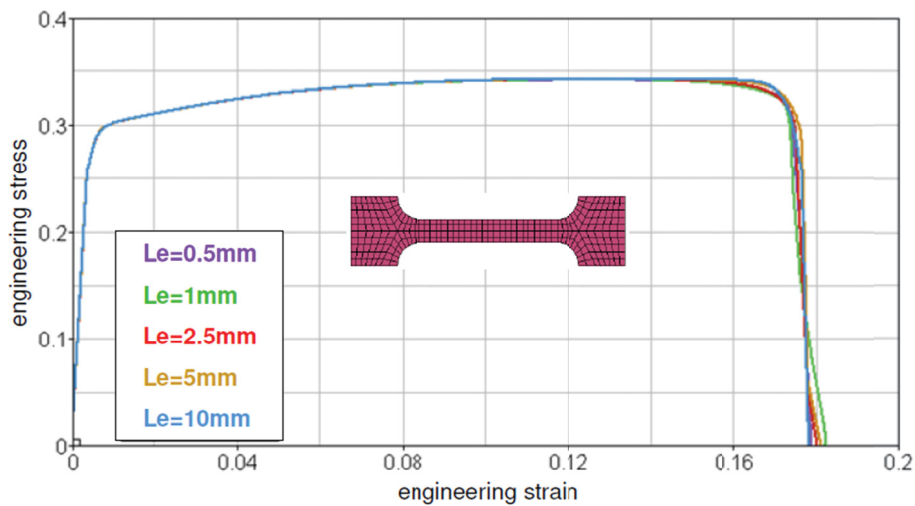


Figure 27: Uniaxial tensile test, regularized stress-strain curves for different element sizes, extracted from [24].

From the LS-DYNA user's manual, the scale curve LCREGD affects the effective plastic strain to failure. Earlier in this report, the failure strain was calibrated by applying an offset to Giglio's failure strain vs. triaxiality curve. While a simple offset may correct the stress-strain curve for a certain loading scenario and mesh size, it is possible that it will give erroneous results for other cases. Another approach would be to use an FEA-based correction factor. Therefore, the failure vs. triaxiality curve's offset was eliminated from the simulations, and the focus became to obtain the correct post-critical behavior using the scale and fading exponents.

Previous simulations in the present work used a constant scaling factor of 1. The simulation results below implemented Haufe's scale curve at different offsets. It should be noted that these are the last simulations that used Giglio's offset failure vs. triaxiality curve.

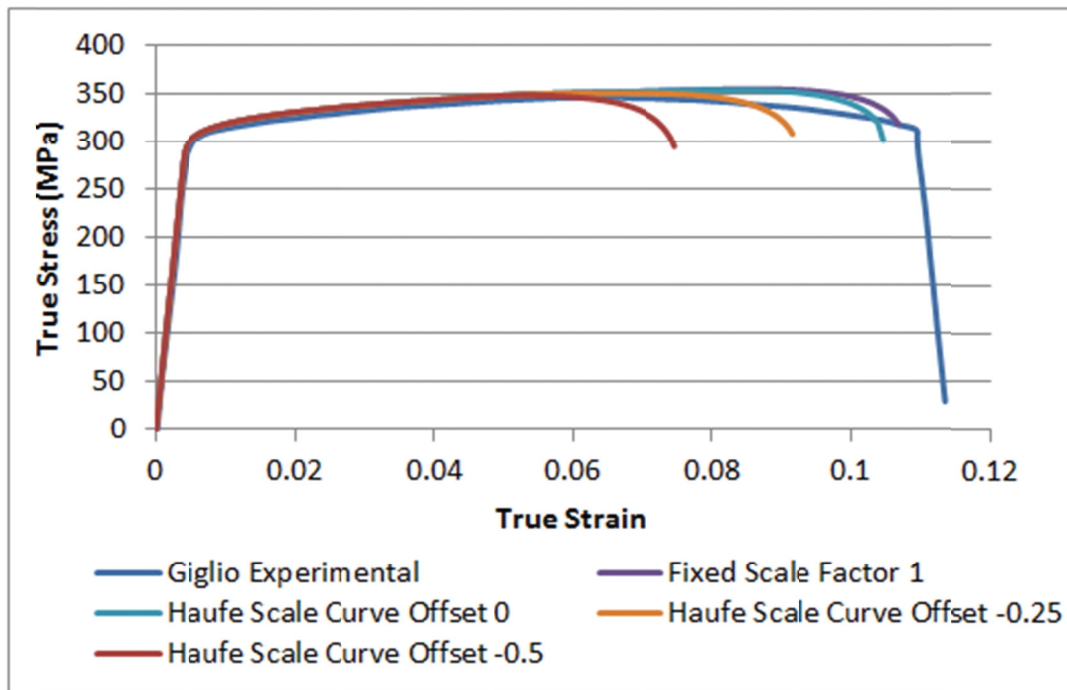


Figure 28: *Effect of implementing Haufe's scale curve with negative offset.*

In Figure 28, it can be seen that scaling the curve has a large effect on the failure strain, even larger than when an offset was applied to the triaxiality curve. In figure 29, a second group of Haufe scale curve experiments using positive offsets is demonstrated.

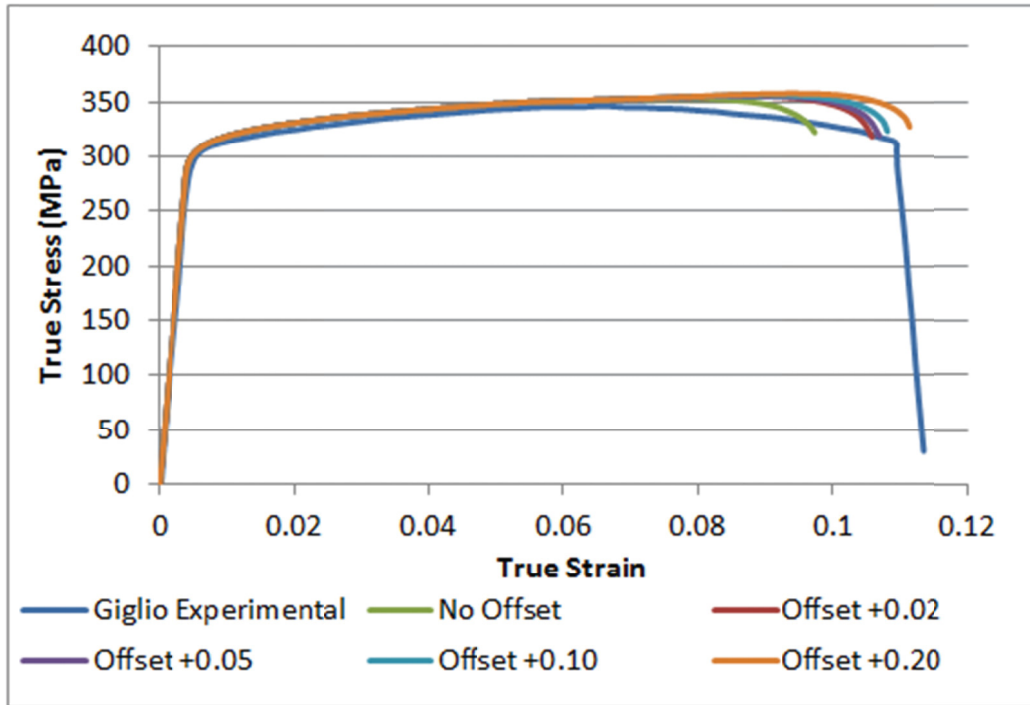


Figure 29: Effect of Implementing Haufe's scale curve with a positive offset.

The offsets that give the best results are +0.1 and +0.2. For fading exponent calibrations, the 0.2 scale curve offset will be preserved.

4.3.7 Seventh trials: Adjusting the fading exponent curve FADEXP

Figures 30 and 31 present respectively the effect of offsetting the fading curve and modifying the FADEXP parameter.

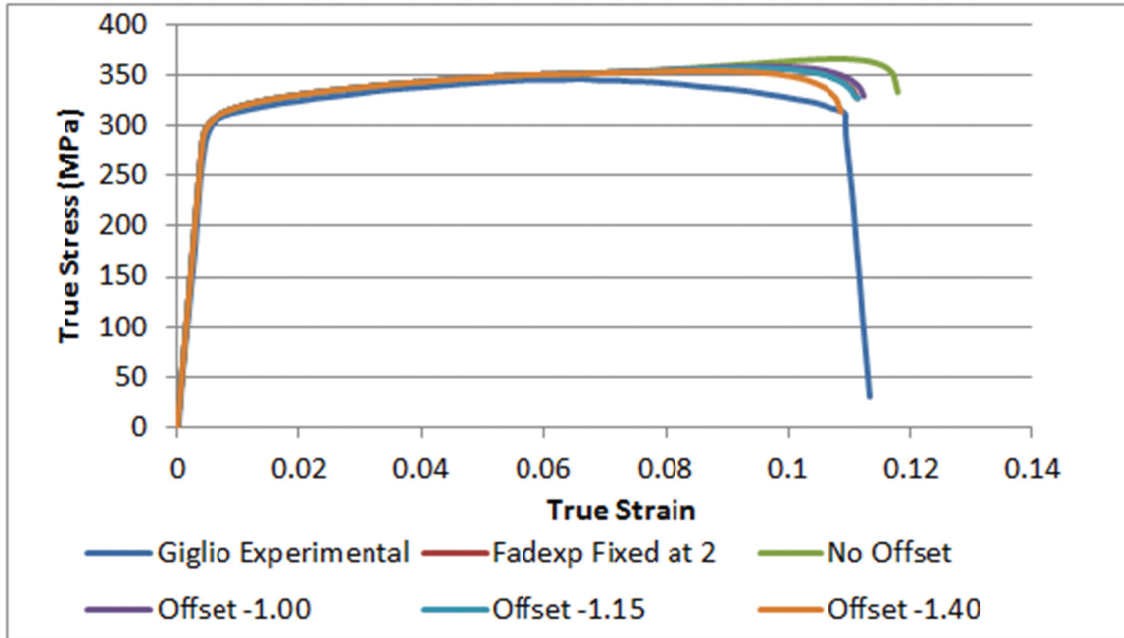


Figure 30: Effect of the fading curve offset.

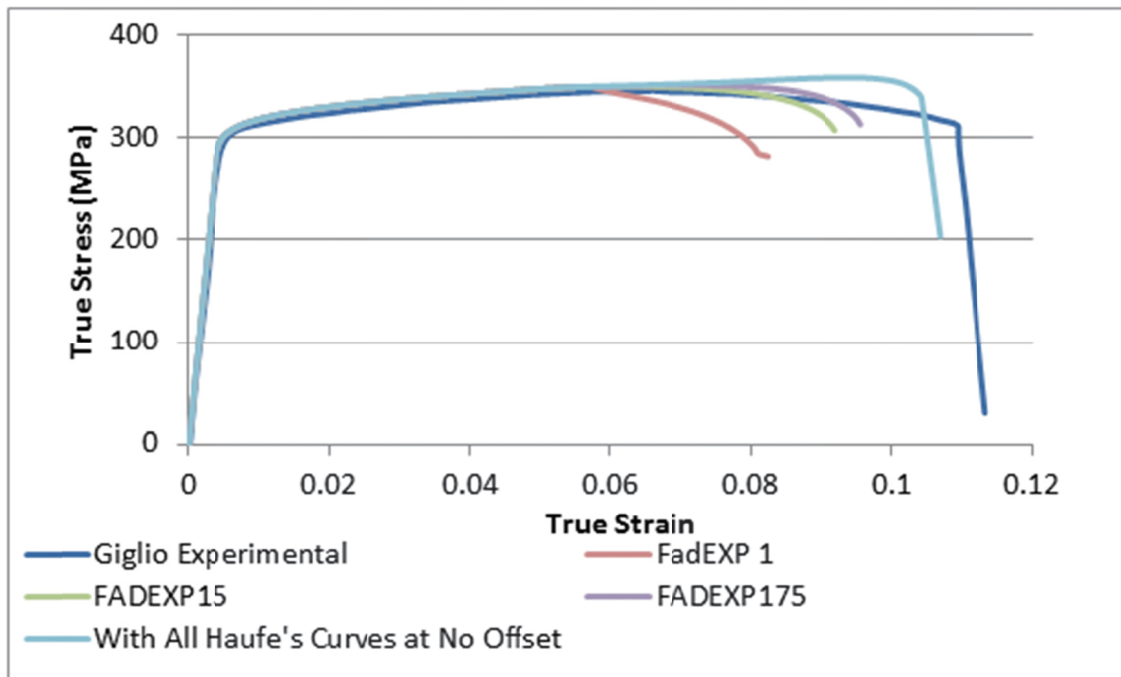


Figure 31: Effect of the FADEX parameter.

4.3.8 Eighth trials: Damage exponent variation

The damage exponent corresponds to the “n” in the GISSMO damage equation [4], reproduced below:

$$\Delta D = \frac{n}{\epsilon_f(\eta)} D^{(1-\frac{1}{n})} \Delta \epsilon_p \quad (54)$$

Previous simulations were performed using a damage exponent of 2. In the following ones, values of 0.1, 1 and 3 were used. These values were chosen arbitrarily in order to evaluate their effects on the true stress-strain curves. The initial value of 2 used previously was taken from Haufe's work [38].

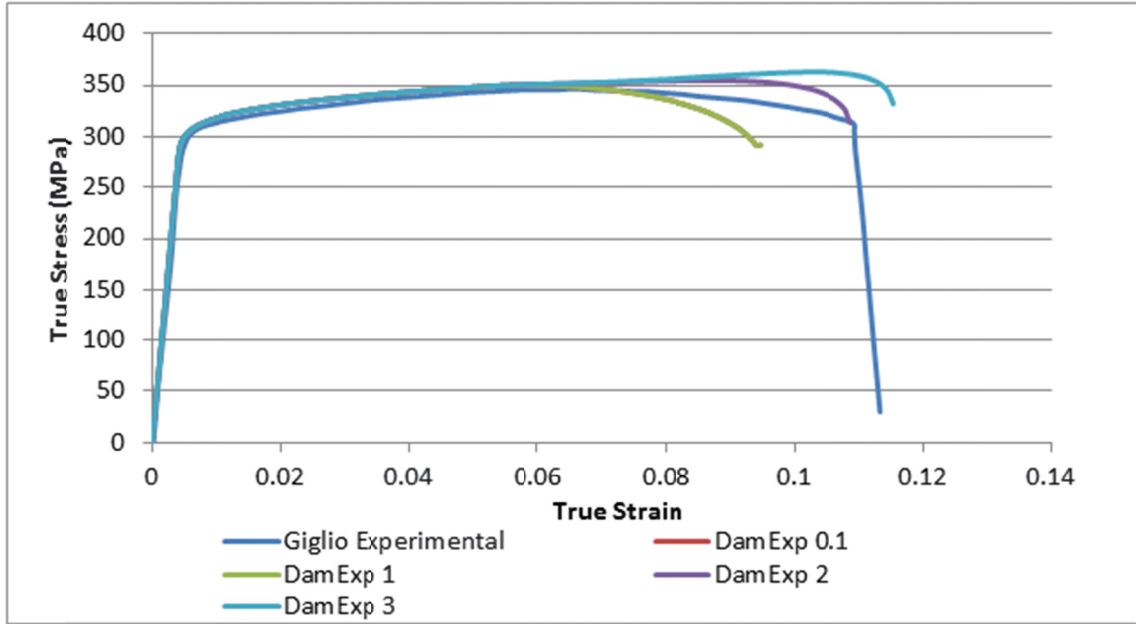


Figure 32: Effect of damage exponent parameter on the true stress-strain curve.

Figure 32 demonstrates that an increase in the damage exponent leads to an increase in the stress and strain at failure. The most accurate simulation remains the one with a damage exponent of 2.

4.4 Summary of numerical simulations

In this section, a numerical model was created and simulations were performed with LS-DYNA hydrocode [1] in order to reproduce a tensile test from Giglio et al. [2]. Simulations of a quasi-static tensile test at room temperature were performed using two constitutive models: the *mat_plastic_kinematic* and the *mat_johnson_cook* model. The effects on the true stress-strain curves of two parameters and of four parameters were investigated respectively. Then, the Johnson-Cook constitutive model was combined to the Generalized Incremental Stress State dependant damage MOdel (GISSMO) that considers damage evolution and effective plastic strain at failure at various triaxialities. Again, the effects on the true stress-strain curves of many parameters were studied. The simulations demonstrated that different combinations of parameters can be used in order to reproduce the true stress-strain behavior during a quasi-static tensile test. However, in order to be able to compare the complete true stress strain curves of the specimens, some information would be required on the instantaneous area of the specimen between the beginning of necking until the failure of the specimen. Also, the influence on the mesh dependency should be considered in further studies. In order to improve the calibration of the GISSMO

parameters, the simulations should be extended to include other types of loading in order to obtain results under different triaxialities. Finally, simulations should be performed and compared with a blast/ballistic impact experiment.

The methodology developed could be used for other materials however; the strain rate components should be considered when the materials are strain rate sensitive to extreme loads.

5 Conclusion

The development of novel concepts and designs of military platforms is increasingly becoming dependant on modeling and simulations that are performed to support their development. Therefore, it becomes essential to predict adequately the damage and failure that occur in the materials when evaluating the dynamic behavior of military protection systems under extreme loads such as against threats effects.

The objective of this report was to find a reliable method to simulate using the LS-DYNA hydrocode the behavior, damage and failure of Aluminium 6061-T6 and to investigate the effect of modifying several constitutive and damage parameters on the numerical behavior. Since this material is considered strain rate insensitive in the strain rates we are interested, results from a quasi-static experimental test from Giglio et al. [2] experiments was used as a reference to compare with the simulations results.

Parameters of the *mat_plastic_kinematic* and of the *mat_johnson_cook* constitutive models were evaluated as well as the effect of modifying several of these parameters when combining to the Generalized Incremental Stress State dependant damage MOdel (GISSMO). Simulations demonstrated that different combinations of parameters can be used in order to reproduce the true stress-strain behavior during a quasi-static tensile test.

The Johnson-Cook constitutive model and Generalized Incremental Stress State dependant damage MOdel (GISSMO) were combined and are proposed as a method to simulate the damage and failure of Al 6061-T6. However, since defence applications involve various failure modes, it is recommended that parameters of the constitutive and the damage/failure models, such as the element fading and the scaling exponents available in the GISSMO damage model, should be well calibrated as a function of element size (to evaluate mesh dependency) and under various triaxalities. Finally, in order to validate the use of the material models for defence applications, simulations should be performed and compared with a blast/ballistic impact experiments.

References

- [1] “LSTC, Livermore Software Technology Corporation,” www.lstc.com, last access date September 1, 2016.
- [2] Giglio, M., Gilioli, A. and Manes, A., “Mechanical Behaviour of Al 6061-T6 Aluminium Alloy Under Large Strain and Failure,” Springer-Verlag, Berlin, 2014.
- [3] Collins, G.S., “An Introduction to Hydrocode Modeling,” Imperial College London, London, 2002.
- [4] “LS-DYNA Keyword User’s Manual Volume II: Material Models,” Livermore, California: Livermore Software Technology Corporation, 2015.
- [5] Meyers, M.-A., “Dynamic Behavior of Materials,” New York: John Wiley & Sons Inc., 1994.
- [6] Ugural, A. and Fenster, S., “Advanced Mechanics of Materials and Applied Elasticity,” Saddle River: Pearson Education, 2012.
- [7] ASM International, “Atlas of Stress-Strain Curves,” Materials Park: ASM International, 2002.
- [8] Schwer, L., “Aluminum Plate Perforation: A Comparative Case Study using Lagrange with Erosion Multi-Material Ale, and Smooth Particule Hydrodynamics,” 2009.
- [9] Corona, E. and Reedlunn, B., “A Review of Macroscopic Ductile Failure Criteria,” Sandia National Laboratories, 2013.
- [10] Johnson, G.R. and Cook, W.H., “A constitutive model and data for metals subjected to large strains, high strain rates and high temperatures,” Proc. 7th International Symposium on Ballistics, pp. 541–547, 1983.
- [11] Dyna Support, “From Engineering to True Strain, True Stress,” <http://www.dynasupport.com/howtos/material/from-engineering-to-true-strain-true-stress>, last access date September 1, 2016.
- [12] Banerjee, A., Dhar, S., Acharyya, S., Datta, D. and Nayak, N., “Determination of Johnson Cook Material and Failure Model Constants and Numerical Modelling of Charpy Impact Test of Armour Steel,” *Materials Science & Engineering*, no. 640, pp. 200–209, 2015.
- [13] Lesuer, D.R., Kay, G.J. and Leblanc, M.M., “Modeling Large-Strain, High-Rate Deformation in Metals,” Livermore, Lawrence Livermore National Laboratory, 2001.
- [14] Manes, A., Peroni, L., Scapin, G. and Giglio, M., “Analysis of Strain Rate Behavior of an Al 6061 T6 alloy,” *Procedia Engineering*, no. 10, pp. 3477–3482, 2011.
- [15] Toussaint, G. and Bouamoul, A., “Close-Range Blast Effects on Small Square Clamped Plates Made from Aluminum 6061-T6,” *Journal of Dynamic Behavior of Materials*, 3(1), pp. 83–99, 2017.

- [16] Armstrong, R. and Zerilli, F., “Dislocation Mechanics Based Analysis of Material Dynamics Behavior,” *Journal de Physique Colloques*, 49 (C3), pp. C3–529–C3–534, 1988.
- [17] Gao, C. and Zhang, L., “Constitutive modelling of plasticity of fcc metals under extremely high strain rates,” *International Journal of Plasticity*, vol. 32–33, no. 2012, pp. 121–133, 2011.
- [18] “Structures of metals,” University of Washington,
https://depts.washington.edu/matseed/mse_resources/Webpage/Metals/metalstructure.htm, last access date August 17, 2017.
- [19] Voyiadjis, G.Z. and Abed, F.H., “Microstructural based models for BCC and FCC metals with temperature and strain rate dependency,” *Mechanics of Materials*, 37, pp. 355–378, 2005.
- [20] Follansbee, P.S. and Kocks, U.F., “A constitutive description of the deformation of copper based on the use of mechanical threshold stress as an internal state variable.” *Acta Metall.* 36, pp. 81–93, 1988.
- [21] Takada, K., Sato, K. and Ma, N., “Fracture Prediction of High Strength Steels with Ductile Fracture Criterion and Strain Dependent Model of Anisotropy,” in *12th International LS-DYNA Users Conference*, Detroit, 2012.
- [22] Lemaitre, J., “A Continuous Damage Mechanics Model for Ductile Fracture,” *Journal of Engineering Materials and Technology*, vol. 107, pp. 83–89, 1985.
- [23] Basaran, M., Wolkerling, S.D., Feucht, M., Neukamm, F. and Weichert, D., “An Extension of the GISSMO Damage Model Based on Lode Angle Dependence,” in *LS-DYNA Anwenderforum*, Bamberg, 2010.
- [24] Effelsberg, J., Haufe, A., Feucht, M., Neukamm, F. and Dubois, P., “On Parameter Identification for the GISSMO Damage Model,” in *Eleventh LS-DYNA Forum*, 2012.
- [25] Andrade, F., Feucht, M. and Haufe, A., “On the Prediction of Material failure in LS-DYNA: A Comparison Between GISSMO and DIEM,” in *13th International LS-DYNA Users Conference*, Dearborn, 2014.
- [26] Corbett, C.J., Laszczyk, L. and Rebuffet, O., “Assessing and validating the Crash Behavior of Securallex HS, a High-Strength Crashworthy Aluminum Alloy, Using the GISSMO Model,” in *14th International LS-DYNA Users Conference*, Dearborn, 2016.
- [27] Borrvall, T., Johansson, T., Schill, M., Jergéus, J., Mattiasson, K. and DuBois, P., “A General Damage Initiation and Evolution Model (DIEM) in LS-DYNA,” in *9th European LS-DYNA Conference 2013*, Manchester, 2013.
- [28] Bao, Y. and Wierzbicki, T., “On Fracture Locus in the Equivalent Strain and Stress Triaxiality Space,” *International Journal of Mechanical Sciences*, no. 46, pp. 81–98, 2004.
- [29] Kut, S., “A Simple Method to Determine Ductile Fracture Strain in a Tensile Test of Plane Specimens,” *Metalurgija*, no. 49, pp. 295–299, 2009.

- [30] Kwon, O.H. and Thompson, M.K., “The Effect of Surface Smoothing and Mesh Density for Single Asperity Contact,” Korea Advanced Institute of Science and Technology, Daejeon, 2011.
- [31] Takaffoli, M., “Experimental and Numerical Study of Single and Multiple Impacts of Angular Particles on Ductile Metals,” Ryerson University, Toronto, 2012.
- [32] Dorbane, A., Ayoub, G., Hamade, R.F. and Imad, A., “Mechanical Response and Evolution of Damage of Al 6061-T6 Under Different Strain Rates and Temperatures,” 2015.
- [33] Kelly, P., “Solid Mechanics Part II: Engineering Solid Mechanics—Small Strain,” http://homepages.engineering.auckland.ac.nz/~pkel015/SolidMechanicsBooks/Part_II/08_Plasticity/08_Plasticity_06_Hardening.pdf, last access date August 18, 2016.
- [34] Berger-Pelletier, H., “Modelling of Split Hopkinson Pressure Bars: Adaptation of a Compression Apparatus into Tension,” Université Laval, Québec City, 2013.
- [35] Brown, L., Joyce, P., Forrest, D. and Wolk, J., “Physical and Mechanical Characterization of a Nano Carbon Infused Aluminum-Matrix Composite,” in *SAMPE Fall Technical Conference*, Fort Worth, 2011.
- [36] Ambriz, R. and Jaramillo, D., “Mechanical Behavior of Precipitation Hardened Aluminum Alloys Welds,” Intech, Azcapotzalco, 2014.
- [37] Lee, W., Sue, W., Lin, C. and Wu, C., “The Strain Rate and Temperature Dependence of the Dynamic impact properties of 7075 Aluminium Alloy,” *Journal of Material Processing Technology*, vol. 100, no. 1–3, pp. 116–122, 2000.
- [38] Haufe, A., Neukamm, F., Feucht, M., DuBois, P. and Borvall, T., “Recent Developments in Damage and Failure Modeling with LS-DYNA,” in *2010 Nordic LS-DYNA Users Forum*, Göteborg, 2010.
- [39] Haufe, A., Dubois, P., Neukamm, F. and Feucht, M., “GISSMO—Material Modeling with a Sophisticated Failure Criteria,” in *LS-DYNA Developer Forum 2011*, Stuttgart, 2011.

List of symbols/abbreviations/acronyms/initialisms

ALE	Arbitrary Lagrangian-Eulerian
BCC	Body Centred Cubic
DDE	Dislocation Density Evolution
DIEM	Damage Initiation and Evolution Model
EOS	Equation of State
ETAN	Tangent Modulus
FCC	Fully Centred Cubic
FLD	Forming Limit Diagram
GISSMO	Generalized Incremental Stress State dependant damage MOdel
HPC	Hexagonal Closed Pack
LOV	Land Operational Vehicles
JC	Johnson Cook
MSFLD	Müschenborn and Sonne Forming Limit Diagram
OFHC	Oxygen-Free High Conductivity
PC	Pressure Cut-off
SALE	Simplified Arbitrary Lagrangian-Eulerian

DOCUMENT CONTROL DATA		
*Security markings for the title, authors, abstract and keywords must be entered when the document is sensitive		
1. ORIGINATOR (Name and address of the organization preparing the document. A DRDC Centre sponsoring a contractor's report, or tasking agency, is entered in Section 8.) DRDC – Valcartier Research Centre Defence Research and Development Canada 2459 route de la Bravoure Québec (Québec) G3J 1X5 Canada		2a. SECURITY MARKING (Overall security marking of the document including special supplemental markings if applicable.) CAN UNCLASSIFIED
		2b. CONTROLLED GOODS NON-CONTROLLED GOODS DMC A
3. TITLE (The document title and sub-title as indicated on the title page.) Constitutive models investigation to simulate damage/failure of Aluminium (Al) 6061-T6		
4. AUTHORS (Last name, followed by initials – ranks, titles, etc., not to be used) Leclerc, P.; Toussaint, G.		
5. DATE OF PUBLICATION (Month and year of publication of document.) November 2018	6a. NO. OF PAGES (Total pages, including Annexes, excluding DCD, covering and verso pages.) 54	6b. NO. OF REFS (Total references cited.) 39
7. DOCUMENT CATEGORY (e.g., Scientific Report, Contract Report, Scientific Letter.) Scientific Report		
8. SPONSORING CENTRE (The name and address of the department project office or laboratory sponsoring the research and development.) DRDC – Valcartier Research Centre Defence Research and Development Canada 2459 route de la Bravoure Québec (Québec) G3J 1X5 Canada		
9a. PROJECT OR GRANT NO. (If appropriate, the applicable research and development project or grant number under which the document was written. Please specify whether project or grant.)	9b. CONTRACT NO. (If appropriate, the applicable number under which the document was written.)	
10a. DRDC PUBLICATION NUMBER (The official document number by which the document is identified by the originating activity. This number must be unique to this document.) DRDC-RDDC-2018-R198	10b. OTHER DOCUMENT NO(s). (Any other numbers which may be assigned this document either by the originator or by the sponsor.)	
11a. FUTURE DISTRIBUTION WITHIN CANADA (Approval for further dissemination of the document. Security classification must also be considered.) Public release		
11b. FUTURE DISTRIBUTION OUTSIDE CANADA (Approval for further dissemination of the document. Security classification must also be considered.)		
12. KEYWORDS, DESCRIPTORS or IDENTIFIERS (Use semi-colon as a delimiter.) Damage; Failure; Constitutive model; 6061-T6		

The design of a military vehicle is a complex science that requires the careful consideration of factors, such as armour protection that is essential for survivability, while considering the need to conceive a lightweight and economical vehicle. Therefore, predicting the material behavior and damage until failure is of primary importance when evaluating the vulnerability of military platforms and could influence the optimization of protection systems. In this report, the aim is to investigate the effect of modifying several constitutive and damage models that could be used to simulate the damage behavior of Aluminium (Al) 6061-T6 using the LS-DYNA hydrocode. Several models are compared numerically and their strengths/weaknesses are presented. The Johnson-Cook constitutive model and GISSMO damage models were combined and the effects of varying several parameters are presented. Since defence applications involve several failure modes, further studies should be performed to investigate the material response under various triaxialities and the mesh dependency in order to simulate accurately the damage/failure of Aluminium 6061-T6.

La conception d'un véhicule militaire est une science complexe qui requiert un examen approfondi de facteurs, tels que l'armure de protection qui est essentiel à la surviabilité, tout en considérant le besoin de concevoir un véhicule léger et économique. C'est pourquoi, prédire le comportement et le dommage jusqu'à la rupture des matériaux est de première importance lorsqu'on évalue la vulnérabilité de plateformes militaires et peut ainsi influencer l'optimisation des systèmes de protection. Dans ce rapport, l'objectif est d'investiguer plusieurs modèles constitutifs et d'endommagement qui pourraient être utilisés pour simuler l'endommagement de l'Aluminium 6061-T6 avec l'hydrocode LS-DYNA. Plusieurs modèles sont comparés numériquement et leurs forces/faiblesses sont présentées. Le modèle constitutif de Johnson-Cook a été combiné au modèle d'endommagement de GISSMO et l'effet de varier la valeur de plusieurs paramètres est présenté. Étant donné que les applications militaires impliquent plusieurs modes de rupture, des études complémentaires devraient être réalisées pour investiguer la réponse du matériau soumis à des triaxialités différentes et la dépendance au maillage dans le but de simuler adéquatement l'endommagement/rupture de l'Aluminium 6061-T6.